



Key Points:

- Ocean extremes characterized by exceptionally low pH and aragonite saturation states (OAXs) are identified and tracked in space and time
- In the California current system, 3% of OAXs are large coherent structures that last for several years and can propagate over 3,000 km
- A quarter of OAXs are characterized by corrosive conditions likely causing dissolution of the shell of marine calcifiers such as pteropods

Supporting Information:

Supporting Information may be found in the online version of this article.

Correspondence to:

F. Desmet,
flora.desmet@usys.ethz.ch

Citation:

Desmet, F., Gruber, N., Köhn, E. E., Münnich, M., & Vogt, M. (2022). Tracking the space-time evolution of ocean acidification extremes in the California current system and northeast Pacific. *Journal of Geophysical Research: Oceans*, 127, e2021JC018159. <https://doi.org/10.1029/2021JC018159>

Received 22 OCT 2021

Accepted 14 APR 2022

Author Contributions:

Conceptualization: Flora Desmet, Nicolas Gruber, Eike E. Köhn
Data curation: Flora Desmet
Formal analysis: Flora Desmet
Funding acquisition: Nicolas Gruber
Methodology: Flora Desmet, Nicolas Gruber, Matthias Münnich, Meike Vogt
Software: Flora Desmet, Eike E. Köhn
Visualization: Flora Desmet
Writing – original draft: Flora Desmet

© 2022. The Authors.

This is an open access article under the terms of the Creative Commons Attribution-NonCommercial-NoDerivs License, which permits use and distribution in any medium, provided the original work is properly cited, the use is non-commercial and no modifications or adaptations are made.

Tracking the Space-Time Evolution of Ocean Acidification Extremes in the California Current System and Northeast Pacific

Flora Desmet¹ , Nicolas Gruber¹ , Eike E. Köhn¹ , Matthias Münnich¹ , and Meike Vogt¹

¹Environmental Physics, Institute of Biogeochemistry and Pollutant Dynamics, ETH Zurich, Zürich, Switzerland

Abstract Ocean acidification is punctuated by episodic extremes of low pH and saturation state with regard to aragonite (Ω_A). Here, we use a hindcast simulation from 1984 to 2019 with a high-resolution regional ocean model (ROMS-BEC) to identify and track ocean acidification extremes (OAX) in the northeast Pacific and the California current system (CCS). In the first step, we identify all grid-cells whose pH and Ω_A are simultaneously below their first percentile over the analysis period (1984–2019). In the second step, we aggregate all neighboring cells with extreme conditions into three-dimensional time evolving events, permitting us to track them in a Lagrangian manner over their lifetime. We detect more than 22 thousand events that occur at least once in the upper 100 m during their lifetime, with broad distributions in terms of size, duration, volume, and intensity, and with 26% of them harboring corrosive conditions ($\Omega_A < 1$). By clustering the OAXs, we find three types of extremes in the CCS. Near the coast, intense, shallow, and short-lasting OAXs dominate, caused by strong upwelling. A second type consists of large and long-lasting OAX events that are associated with westward propagating cyclonic eddies. They account for only 3% of all extremes, but are the most severe events. The third type is small extremes at depth arising from pycnocline heave. OAXs potentially have deleterious effects on marine life. Marine calcifiers, such as pteropods, might be especially impacted by the long-lasting events with corrosive conditions.

Plain Language Summary The emission of carbon dioxide by human activities causes ocean acidification (OA), that is, the decrease of the pH and saturation level of seawater with respect to the carbonate mineral aragonite. Episodic events of unusually low pH and aragonite saturation level punctuate these long-term declines, potentially intensifying stress on marine plankton. Particularly prone to extremes is the California current system off the U.S. West Coast due to its naturally low pH-aragonite waters and its strong variability. We use a high-resolution numerical model to identify and characterize extreme events associated with OA in this region, and understand their drivers. We find extremes to have a broad range of volumes, durations, and strengths, with a quarter of them carrying corrosive conditions for shelled organisms, that is, aragonite saturation levels below 1. The largest and longest-lived events are associated with cyclonic eddies (whirls of approximately 50–100 km in diameter) that trap upwelled low pH-aragonite waters near the coast. Although representing only 3% of the events, they cause most of the total excess of acidity induced by all identified extremes. The vertical extent and duration of extremes with corrosive mean conditions are expected to impact calcifying organisms, such as pteropods.

1. Introduction

While long-term trends in ocean acidification (OA) are well characterized and studied (Bates et al., 2014; Bopp et al., 2013; Doney et al., 2009; Feely et al., 2012; Jiang et al., 2019; Lauvset et al., 2015; Orr et al., 2005), comparatively little is known about the characteristics, distribution, drivers, and impacts of OA extremes, that is, episodic and short-term anomalies of the different parameters characterizing the ocean's carbonate chemistry system (Burger et al., 2020; Gruber et al., 2021; Hauri, Gruber, McDonnell, & Vogt, 2013). By definition, the chemical conditions during such OA extremes are highly unusual, with respect to both today and the past. Given that OA trends will continue into the future as long as atmospheric CO₂ keeps rising, these OA extremes may offer a glimpse into the future, when such extreme conditions could become the norm. In addition, compared to the more slowly evolving impacts of the long-term trends in OA on OA sensitive marine organisms, OA extremes may hit these communities harder and be more disruptive to ecosystems (Engström-Öst et al., 2019; Kroeker et al., 2020; Lohbeck et al., 2012; Riebesell & Gattuso, 2015). Since extremes develop much more rapidly, there

Writing – review & editing: Flora Desmet, Nicolas Gruber, Eike E. Köhn, Matthias Münnich, Meike Vogt

is little time for organisms to employ coping strategies in response to change (Gruber et al., 2021). Besides, extremes interfere with physiological and ecological processes on exactly the daily to monthly timescales that are most relevant to these processes (Kroeker et al., 2020).

So far, only a handful of studies have investigated OA extremes, both on the regional (Hauri et al., 2015; Hauri, Gruber, McDonnell, et al., 2013) and the global scale (Burger et al., 2020; Gruber et al., 2021). All of them pointed out that the long-term trend in OA leads to a rapid and strong increase in the number, duration, extent, and intensity of OA extremes. However, the definition of what constitutes an OA extreme substantially differs across studies, since there is no consensus yet with respect to the many choices that need to be taken in order to define such an extreme (Gruber et al., 2021). A first choice concerns the carbonate chemistry variable of interest, that is, Ω_A (Hauri, Gruber, McDonnell, et al., 2013), pH or hydrogen ion concentration ($[H^+]$; Burger et al., 2020; Gruber et al., 2021), where $\Omega_A = ([Ca^{2+}][CO_3^{2-}]/K_{sp}^*$, with K_{sp}^* representing the solubility product of aragonite, and $pH = -\log[H^+]$). A second choice concerns the threshold used to define which conditions are extreme, and thus likely to affect biological processes from the cellular to the macroecological scale (Gruber et al., 2021). This threshold can be an absolute value (Hauri, Gruber, McDonnell, et al., 2013) or be defined in relative terms, that is, based on a percentile value of the cumulative distribution (Burger et al., 2020; Gruber et al., 2021). For the former (absolute) approach, relevant thresholds vary between species and taxonomic groups, life stages, physiological functions considered (e.g., Bednaršek et al., 2019; Busch & McElhany, 2016; Cripps et al., 2014; Fabry et al., 2008, and references therein) and have also been found to depend on the state of other co-stressors (e.g., Seifert et al., 2020). For the latter (relative) approach, the threshold can be calculated based on a fixed baseline, where the cumulative distribution is determined from the data over a given time period, or based on a shifting or time-evolving baseline, where the underlying data are either detrended/smoothed or the reference period shifts with time (Burger et al., 2020; Gruber et al., 2021; Oliver et al., 2021). The third choice concerns the spatiotemporal analysis framework, that is, whether one looks at extreme conditions at a fixed location (Eulerian approach), or whether one follows extremes as distinct volumes propagating and distorting through space and time (Lagrangian approach). All three choices need to be motivated by the consideration of the associated biological impacts on marine organisms.

As changes in pH ($[H^+]$) and Ω_A have different biological effects, the choice of the carbonate chemistry variable to focus on when investigating OA extremes remains debated (Bednaršek et al., 2019; Doney et al., 2009, 2020; Kleypas et al., 2006; Kroeker et al., 2013). Many reviews have summarized observational evidence from (multiple) stressor research across a wide range of benthic and pelagic taxa and physiological functions (Busch & McElhany, 2016; Fabry et al., 2008; Kleypas et al., 1999; Kroeker et al., 2010, 2013). Different marine taxa have been shown to respond to different carbonate variables, with some taxa being sensitive to variations in multiple variables. Taking the abundant and well-studied zooplankton calcifiers group of the pteropods as an example, Ω_A has been shown to control the dissolution rates, shell growth, and survival of shelled pteropods (Bednaršek et al., 2019, 2014, 2017). pH ($[H^+]$), in turn, has been shown to affect the embryonic development of pteropods, and the abundance, size, and carbon content of pteropods eggs (Manno et al., 2016). Hence, pteropods have been shown to be impacted by both low pH and low Ω_A during different life stages, with adults responding to Ω_A , and pteropod eggs to pH.

Since carbonate parameters such as pH and Ω_A also often covary in experimental studies on the impact of OA on marine organisms (Comeau et al., 2012, 2010; Mekkes et al., 2021; Spisla et al., 2021), the leading driver cannot always be reliably identified (Bach, 2015). Hence, the use of a combined pH- Ω_A metric may prove useful to identify OA extremes that are likely to affect (a) a range of marine taxa that are sensitive to either one of these drivers, (b) species where both variables affect different life stages, or (c) species where the lead driver currently cannot be unequivocally identified.

With regard to the second choice, both absolute and relative thresholds have been used to define OA extreme conditions in previous studies. The absolute threshold of $\Omega_A = 1$ is particularly useful to characterize the onset and spread of corrosive ($\Omega_A < 1$) conditions (Hauri et al., 2015; Hauri, Gruber, McDonnell, et al., 2013), which are clearly harmful to all calcifying organisms. However, this threshold choice misses OA extremes in waters that remain supersaturated ($\Omega_A > 1$). In fact, biological effects of OA have been shown to occur well above the saturation threshold for aragonite, $\Omega_A = 1$, depending on the species and life stages considered (Bednaršek et al., 2019). An alternative is to use a relative (percentile) threshold, supported by the argument that organisms tend to be adapted to their local environment and its variability (Cornwall et al., 2020; Kroeker et al., 2020; Rivest

et al., 2017; Vargas et al., 2017). One thus expects the rareness of the conditions to play an important role in what organisms experience as extreme. In light of this, Burger et al. (2020) analyzed high acidity extremes using the first percentile of daily $[H^+]$ values as the threshold. Furthermore, they used a shifting baseline in order to remove long-term trends in acidification prior to detecting the extremes. The assumption underlying the choice for such a shifting baseline is that marine ecosystems can adapt to the relatively slowly evolving mean changes in acidification, but that extremes occur too rarely and happen too rapidly in order for organisms to cope (see also Gruber et al., 2021; Oliver et al., 2021). However, the level of adaptive capacity of marine ecosystems to long-term changes in OA is still unclear (Bednaršek et al., 2016, 2017, 2021; Manno et al., 2017; Mekkes et al., 2021). The possible lack of adaptive strategies of some marine populations may lead to episodic crossings of biological thresholds (Bednaršek et al., 2017; Doney et al., 2020). The use of a percentile-based threshold defined on a fixed baseline captures OA extremes that emerge from the combination of long-term anthropogenic changes and decadal to daily variability changes.

The third and final choice concerns the frame of reference, that is, an Eulerian vs. a Lagrangian perspective. So far, all modeling studies on OA extremes have taken an Eulerian approach. Focusing on Ω_A extreme events on the continental shelf of the U.S. West Coast, Hauri, Gruber, McDonnell, et al. (2013) found a fourfold increase in the number of undersaturation ($\Omega_A < 1$) events between the preindustrial era and 2010, as well as a lengthening of their duration. The same Eulerian approach was used by Hauri et al. (2015) for the Southern Ocean, highlighting the imminent emergence of undersaturated conditions in the near-surface ocean in this critical oceanic region. Recently, Burger et al. (2020) took a step forward by considering OA extremes as three-dimensional structures. They achieved this by spatially aggregating connected grid-cells with extreme conditions to assess the spatial extent of these events (see also Gruber et al., 2021). However, Burger et al. (2020) kept an Eulerian approach to study the intensity and duration of an OA extreme.

Both Eulerian and Lagrangian approaches have their strengths and weaknesses. The Eulerian perspective is certainly the more appropriate approach to study the impact of OA extremes on benthic organisms and ecosystems that are fixed in place. However, it misses the potential propagation of OA extremes in space and time, induced by for example, ocean currents, planetary waves, or propagating mesoscale eddies. Yet, knowledge of the space-time dynamics of OA extremes is required to match the physiological or the ecological dynamics of floating or drifting organisms that are trapped within such moving events (Bednaršek et al., 2017; Hauss et al., 2016; Kroeker et al., 2020). Thus, for open ocean studies on OA extremes, their spatiotemporal movement, their drivers, and their impacts, a Lagrangian approach appears to be the more appropriate choice.

Eastern boundary upwelling systems (EBUS) are model systems for OA extremes research, due to the natural high variability of their carbonate chemistry (Fassbender et al., 2011, 2018; Hauri, Gruber, McDonnell, et al., 2013; Leinweber & Gruber, 2013; Torres et al., 2021; Turi et al., 2014) and their highly productive waters (Messié et al., 2009; Pauly & Christensen, 1995). The California current system (CCS) constitutes one of the world's four major EBUS (Chavez & Messié, 2009) and has been extensively studied in the last decades due to its vulnerability with regard to ongoing long-term OA (Chan et al., 2017; Feely et al., 2008; Gruber et al., 2012; Hauri, Gruber, McDonnell, et al., 2013; Hauri et al., 2009; Hauri, Gruber, Vogt, et al., 2013; Turi et al., 2016). The depth of the aragonite saturation horizon, that is, the depth where $\Omega_A = 1$, has been shown to reach occasionally the near-surface waters of the CCS (Feely et al., 2008, 2016), reflecting, in part, a shoaling trend of about 33 m per decade in the CCS from 1979 to 2012 attributed to both anthropogenic carbon accumulation and natural decadal climate variability over the 34 yr period (Turi et al., 2016). Concurrently, the average Ω_A and pH in the top 60 m of the CCS water column decreased by ~0.1 and 0.02 per decade, respectively (Osborne et al., 2020; Turi et al., 2016). OA has been suggested to threaten the highly productive California current ecosystem and its associated blue economy (Cooley & Doney, 2009; Ekstrom et al., 2015; Marshall et al., 2017), with many native taxa under pressure (Busch & McElhany, 2016). For instance, in the pelagic realm, the negative effect of OA on pteropods, an abundant group in the top 100 m of the CCS waters and important element of the CCS food web (Bednaršek et al., 2012, 2014, 2017; Bednaršek & Ohman, 2015), may have cascading repercussions on higher trophic levels (Haigh et al., 2015; Marshall et al., 2017).

The vulnerability of the CCS to acidification largely stems from the fact that it is a system with intrinsically low pH and Ω_A due to the seasonal upwelling of thermocline waters along the continental shelf into the euphotic zone (Checkley & Barth, 2009; Feely et al., 2008; García-Reyes & Largier, 2010; Gruber et al., 2012). Waters below the thermocline are older and have accumulated the products of organic matter remineralization over long

time scales, leading to naturally high dissolved inorganic carbon (DIC) concentrations, as well as naturally low pH and Ω_A . Complex interacting biogeochemical and physical mechanisms modify the chemical composition of the upwelled waters before, during, and after their upwelling, generating a highly variable mosaic of pH and Ω_A conditions (Cai et al., 2020; Hauri, Gruber, Vogt, et al., 2013). In addition to its upwelling regime, the CCS is characterized by extensive mesoscale eddy and filament activity (Frenger et al., 2018; Kurian et al., 2011; Strub & James, 1995; Strub et al., 1991). Through the process termed eddy-pumping, cyclonic eddies lift the thermocline upwards in their eddy core (Chenillat, 2015; Chenillat et al., 2016), which simultaneously causes an uplift of low pH- Ω_A waters. Additionally, mesoscale eddies and filaments have been shown to trap upwelled waters and transport them in a relatively isolated manner hundreds of kilometers offshore (Amos et al., 2019; Frischknecht et al., 2018; Nagai et al., 2015).

In the present study, we use results from a Pacific basin-scale high-resolution oceanic model (ROMS-BEC) simulation, together with a newly developed Lagrangian tracking and analysis method, in order to quantify the number, size, duration, intensity, and propagation properties of OA extremes from 1984 to 2019. We identify extremes by requiring them to be locally anomalously low in both pH and Ω_A simultaneously, using the entire analysis period (1984–2019) as the reference period. For the first time, we adopt a Lagrangian framework for the study of OA extremes. We identify the extremes across the upper 150 m, but then focus only on those that occupy at least once in their lifetime the biomass-rich upper 100 m. We will refer to these OA extremes as OAX. OAXs with similar properties are grouped together using a cluster analysis. We then elucidate the relative roles of the above physical processes in driving extremes of each group. We thereby expect that the same processes contributing to the spatiotemporal variability of pH and Ω_A are also key for the formation of OAX.

2. Methods

2.1. Coupled Regional Ocean Modeling System (ROMS-BEC)

We use the UCLA-ETH version of the Regional Ocean Modeling System (ROMS; Frischknecht et al., 2018; Marchesiello et al., 2003; Shchepetkin & McWilliams, 2005). The model uses a telescopic grid that covers the whole Pacific basin centered on one pole at the U.S. West Coast (Frischknecht et al., 2018). The horizontal grid resolution ranges from 4 km off central California to 60 km around Australia. The telescopic grid allows the model to fully resolve mesoscale dynamics in the CCS, while capturing basin-wide oceanic and atmospheric teleconnections at reasonable computational costs. In the vertical, our setup uses 64 terrain-following vertical coordinates.

Coupled to the physical component is the biogeochemical/ecosystem model BEC (Frischknecht et al., 2018; Moore et al., 2013). BEC simulates the cycling of carbon and four nutrients (P, N, Si, and Fe), which support the growth of three phytoplankton functional types grazed by a single zooplankton type. The produced organic matter is subject to remineralization and vertical export, modeled here explicitly by considering the vertical sinking and advective transports of particles (Frischknecht et al., 2018). Overall, 38 tracers are simulated, including DIC and alkalinity (Alk) required to fully represent the marine carbon cycle. CaCO_3 production, that is, calcification, is a varying fraction of the net primary production by small phytoplankton. The fraction is initiated at 5.5% of the small phytoplankton production and varies depending on nutrient, temperature, and small phytoplankton biomass levels, with a maximum possible fraction of 40% (Moore et al., 2002). The resulting $\text{CaCO}_3:\text{C}$ stoichiometric ratio is used to calculate CaCO_3 losses through grazing, mortality, and aggregation. The organic matter associated with CaCO_3 remineralizes at a rate of 0.0625 days⁻¹ and sinks by 25 m days⁻¹, following the explicit sinking parametrization of Frischknecht et al. (2018). This represents a dissolution length scale of about 400 m.

The properties pH (on the total scale) and Ω_A are computed offline using the MOCSY 2.0 routine (Orr & Epitalon, 2015) and the constants recommended by Dickson et al. (2007). The dissociation constants of carbonic acid K_1 and K_2 follow the Lueker et al. (2000) formulation; the equilibrium constant K_F for hydrogen fluoride HF follows Perez and Fraga (1987) formulation and Uppström (1974) is used for the computation of the total inorganic boron concentration.

2.2. Forcing

The model is forced by daily surface short and long-wave radiations, wind stress, and surface freshwater fluxes derived from the hourly ERA5 regridded product from 1979 to 2019 (Copernicus Climate Change Service

[C3S], 2017; Hersbach et al., 2020). We apply the Drakkar community correction previously derived for ERA-interim fields (Dussin et al., 2016) to the radiations, as well as a sea-ice correction to the radiations, and wind stress following Frischknecht (2018). Climatological riverine inputs of freshwater are included as well as the atmospheric deposition of N (Frischknecht et al., 2018). Atmospheric CO₂ is provided as a monthly varying boundary condition at every grid point based on the monthly marine boundary layer atmospheric CO₂ mixing ratio product of NOAA (GLOBALVIEW-CO2, 2011), converted by Landschützer et al. (2020) to atmospheric pCO₂ by taking into account atmospheric pressure and the contribution of water vapor (Dickson et al., 2007). As the Landschützer product extends only back to 1982, we use a linear extrapolation to estimate atmospheric CO₂ from 1979 to 1982.

Initial and boundary conditions for DIC and Alk are derived from the 1° × 1° GLODAPv2 mapped climatology (Lauvset et al., 2016). DIC is adjusted back to 1969 using the transient steady-state approach and the anthropogenic CO₂ fields of Sabine et al. (2004). The DIC concentrations at the lateral open boundaries in the Southern Ocean evolve transiently based on GLODAPv2 climatological preindustrial DIC and time evolving anthropogenic carbon fields, following the procedures described in detail by Franco et al. (2018).

2.3. Simulation

We spin up the physical component of the model for 10 yr using daily fields from the year 1979. After 10 yr of physical spin-up, we run another 10 yr of spin-up including BEC. During these 10 yr, atmospheric CO₂ and the lateral DIC boundary conditions evolve in a transient manner, representing the linearly extrapolated conditions between 1969 and 1979. We then perform a 41 yr hindcast simulation from 1979 to 2019 using the transient surface forcing and the transient DIC at the southern boundary. The model is integrated with a time step of 600 s and the output is saved at daily resolution. We use daily mean outputs from 1984 to 2019 for our analysis of extreme events.

2.4. Model Evaluation

2.4.1. Ocean Interior pH and Ω_A Distributions

In the climatological mean (1984–2019), ROMS-BEC captures the large-scale interior distribution of Ω_A in the northeast Pacific and especially the spatial pattern of the depth of the aragonite saturation horizon (h_{Ω_A}) with good fidelity (Figure 1a). The simulated depths correlate with a Spearman coefficient of $r = 0.94$ ($n = 203$ 1° × 1° bin-average data points) with the depths derived from the climatological GLODAPv2 1° × 1° gridded Ω_A observational product (Lauvset et al., 2016). The model h_{Ω_A} is on average 15 m shallower than that derived from the observations (Figure 1a), especially in the central CCS, where the difference can reach 130 m. The evaluation of the simulated depth of the climatological annual mean pH = 7.9 isosurface against the corresponding GLODAPv2 product reveals the same features (Figure 1b; $r = 0.96$ (Spearman); $n = 204$) with a mean bias of 40 m. However, differences between model and the data product likely arise from differences in spatiotemporal resolution, with the model resolving finer spatial details due to its higher resolution, as well as its sub-monthly scale variability. When evaluating subregional features, especially those associated with coastal settings, the GLODAPv2 product needs to be viewed with caution.

The results of the model evaluation against the climatological surface and interior state of key parameters, namely temperature (NOAA OISST [Reynolds et al., 2007], SODA 1.4.2 [Carton & Giese, 2008]), salinity (SODA 1.4.2), DIC, Alk (GLODAPv2 [Lauvset et al., 2016]), sea surface partial pressure of CO₂ (Landschützer et al., 2020), sea surface pH and Ω_A (OceanSODA-ETHZ [Gregor & Gruber, 2021]), and sea surface chlorophyll-a (GlobColour) confirm the ability of the model to capture the large-scale climatological state of the northeast Pacific (Figures S1–S5 in Supporting Information S1). Interior temperature, salinity, and density fields in the CCS are in good agreement ($r = 0.99$, $r = 0.96$, and $r = 0.99$ [Pearson]) with observations suggesting a good representation of the magnitude of the coastal upwelling by our model. Also, the DIC variations are well captured ($r = 0.93$ [Pearson]), although the model overestimates it in a coastal 80–150 m depth band. As the model overestimates nearshore surface chlorophyll (mean positive bias in the CCS of 0.27 mg m⁻³), this DIC bias could be the result of too strong remineralization in coastal subsurface waters. This is consistent with the underestimation of pH and Ω_A in this region and the overly shallow saturation horizon compared to observations. These biases would cause an

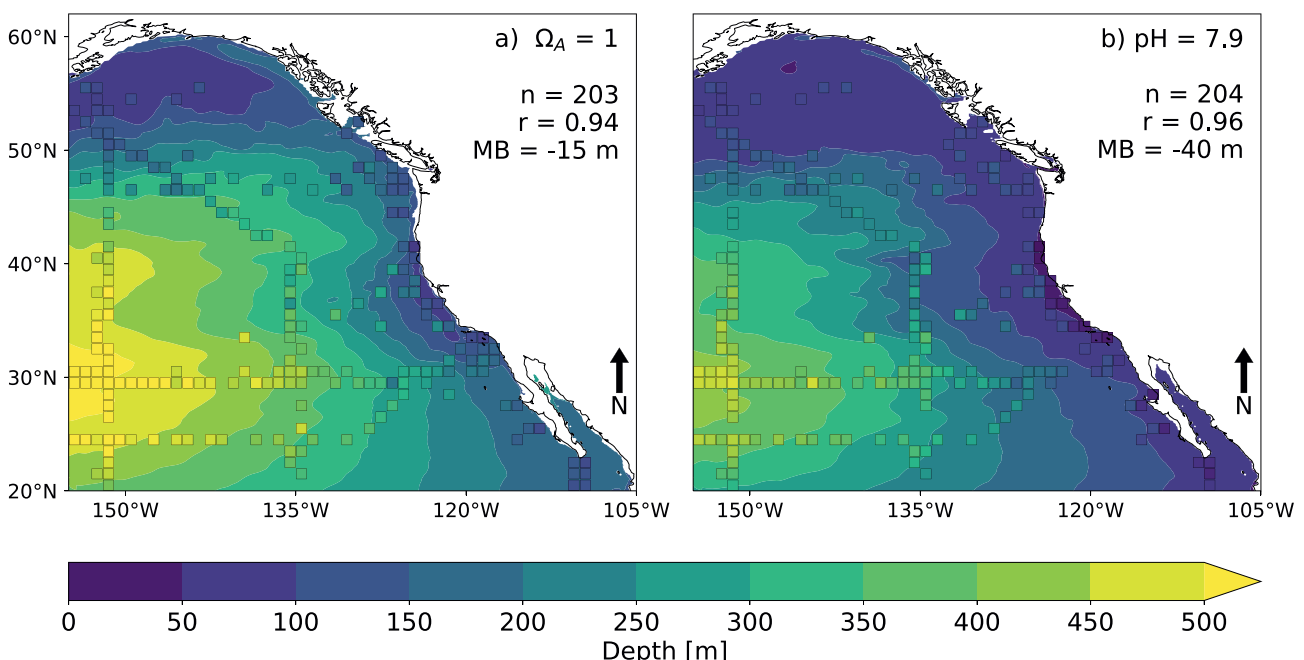


Figure 1. Evaluation of the model simulated annual mean depths of (a) the Ω_A saturation horizon ($\Omega_A = 1$) and (b) the $\text{pH} = 7.9$ isosurface compared to the corresponding observational estimates based on the $1^\circ \times 1^\circ$ gridded GLODAPv2 climatology (Lauvset et al., 2016). The model simulated results are shown as filled contours, while the (gridded but not mapped) observations are shown as filled squares. Each square stands for the corresponding $1^\circ \times 1^\circ$ bin of the gridded product. The corresponding spatial Spearman's correlations (r), spatial mean biases (MB), and number of points (n) used for the calculation are indicated at the top.

overestimation of the number of extremes detected using an absolute threshold on Ω_A for their definition, while they have only a limited impact on the results based on a relative threshold.

Zooming in on the CCS, the evaluation of the interior distribution of modeled pH and Ω_A against bottle data from the North American Carbon Program West Coast Cruise (Feely et al., 2008) further supports the conclusion that the model is well suited to investigate OA in the CCS. The cruise that took place from May to June 2007 covered 13 cross-shelf transects from 24°N to 52°N , with 2,058 pH and Ω_A data points. We match model and cruise data by averaging pH and Ω_A along a 50 km wide band following each transect (Figure 2a) and restrict the evaluation to the upper 150 m of the water column, as our study only considers extreme conditions within the 0–150 m depth layers (Section 2.5). While both interior pH and Ω_A are overestimated in the northern CCS during the time of this cruise (Figures 2b and 2c; Table S1 in Supporting Information S1), the sign of the mean bias varies in the central and southern CCS (Figures 2d–2g, Table S1 in Supporting Information S1). The model simulates a 75 m too deep aragonite saturation horizon in transect 5 (Figure 2b), whereas its depth is underestimated by 31 and 12 m on average in the model in transects 8 and 10 (Figures 2d and 2f). At the same time, the simulated $\text{pH}_{7.9}$ isopleths match the observed ones in all three transects (Figures 2c, 2e and 2g). Rank spatial correlations between interpolated bottle data and model pH and Ω_A interior field remain above 0.8 for 12 transects (Table S1 in Supporting Information S1) suggesting a good representation of the interior pH and Ω_A in our region of interest.

2.4.2. Temporal Variability

We evaluate the temporal variability of the modeled sea surface temperature (SST), pH, and pCO_2 against daily data from three mooring sites off the U.S. West Coast and one in the northeast Pacific subpolar gyre, namely CCE1 ($34.48^\circ\text{N}, 122.51^\circ\text{W}$; $n_{\text{temp}} = 2,325$, $n_{\text{pH}} = 601$, $n_{\text{pCO}_2} = 2,322$ data points), CCE2 ($34.32^\circ\text{N}, 120.81^\circ\text{W}$; $n_{\text{temp}} = 2,433$, $n_{\text{pH}} = 1,012$, $n_{\text{pCO}_2} = 2,431$), Cha'ba ($47.94^\circ\text{N}, 125.96^\circ\text{W}$; $n_{\text{temp}} = 1,430$, $n_{\text{pH}} = 778$, $n_{\text{pCO}_2} = 1,428$) and Papa ($50.13^\circ\text{N}, 144.84^\circ\text{W}$; $n_{\text{temp}} = 3,486$, $n_{\text{pH}} = 2,357$, $n_{\text{pCO}_2} = 3,436$), from 2010 to 2019 (Sutton et al., 2019). We match model and mooring data by binning the 3-hourly mooring data to daily averages and by selecting the closest model grid-cell to the mooring location.

The model captures the observed temporal variability of SST at the four mooring stations, as illustrated by the high (temporal) Spearman correlations of above 0.84 for all sites (Figure 3b). The amplitudes of the simulated

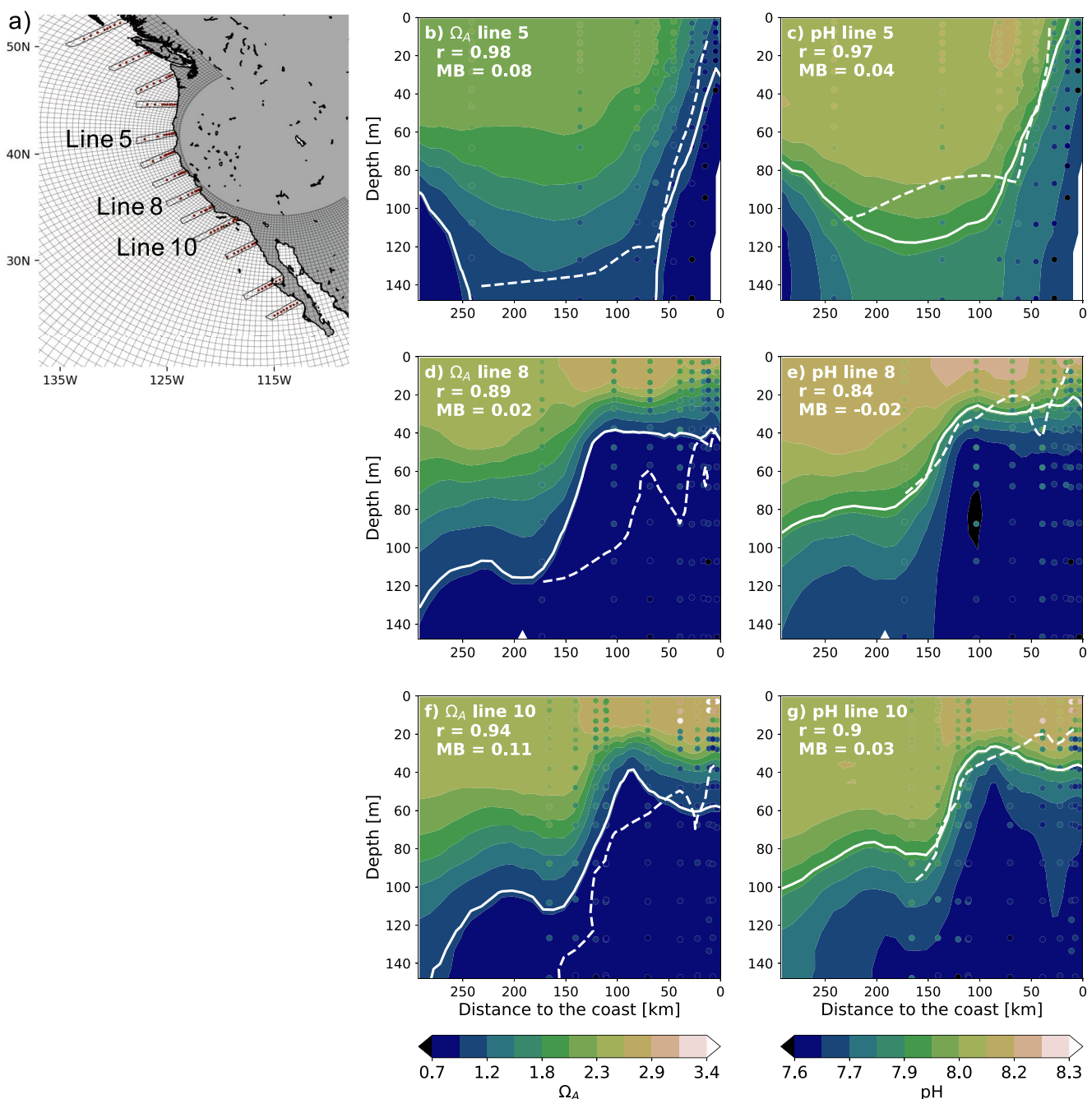


Figure 2. Evaluation of model simulated Ω_A and pH against observations from the North American Carbon Program (NACP) West Coast Cruise (Feely et al., 2008). (a) Map of stations and masks used for simulated fields for each transect, plotted on top of every fifth grid lines of ROMS-BEC grid. (b–g) Offshore transects of (b, d, and f) Ω_A and (c, e, and g) pH at transect 5 (top), 8 (middle), and 10 (bottom) (see map in (a) for locations). The model simulated fields are shown as filled contours, while the observations are shown as filled circles. White lines denote the simulated (solid lines) and observed (dashed) $\Omega_A = 1$ horizon (b, d, and f) and $\text{pH}_{7.9}$ isopleth (c, e, and g), respectively. Spearman spatial correlations (r) and mean biases (MBs) between model and observations of the interior distribution along those transects are given in the top left corners.

daily SST variability are in good agreement with the observed ones across timescales (daily to interannual) and sites (Figures 3b and 3c; simulated standard deviations normalized to observed ones (σ_n) between 1.05 and 1.25 for all sites), with the model tending to overestimate the SST variability (standard deviation can be overestimated by up to 0.48°C in the model (0.33°C on average)). Overall, the timing and magnitude of the daily variability of simulated SST are well-captured, suggesting a good representation of circulation in our model. Simulated surface

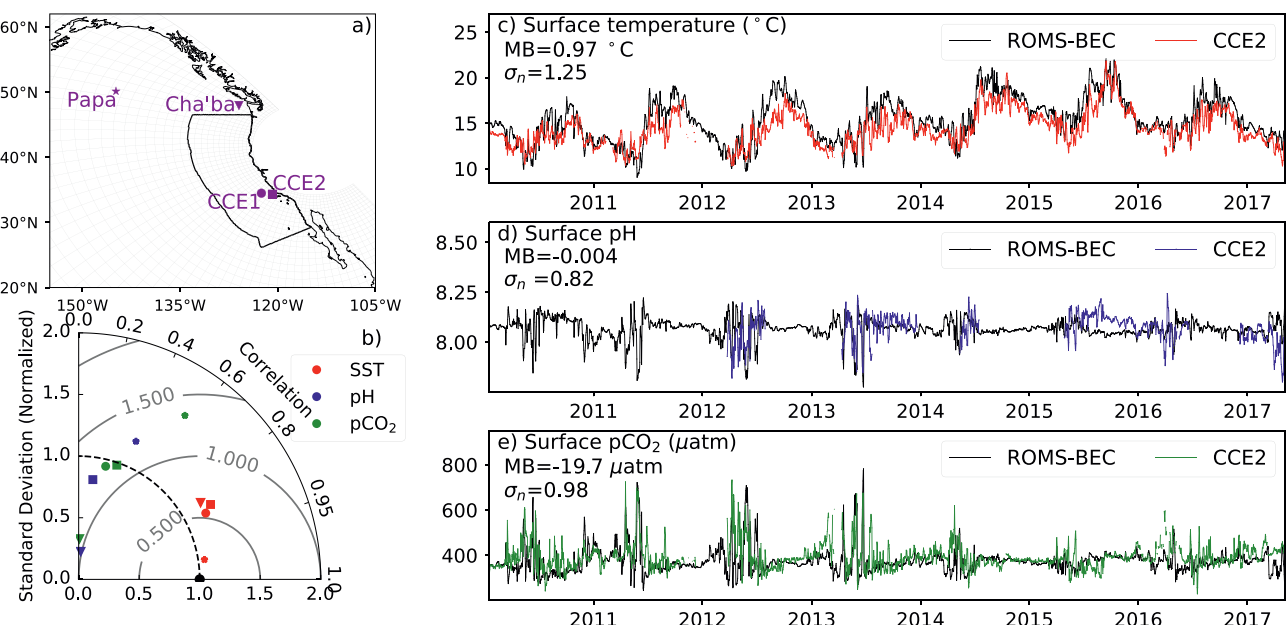


Figure 3. Evaluation of model simulated temporal variability against mooring-based observations. (a) Map of mooring sites used for the evaluation and (b) Taylor Diagrams for sea surface temperature (red), pH (blue), and pCO_2 (green) using Spearman correlations. Each marker shape corresponds to one station in (a). (c–e) Daily time series from 2010 to 2017 at station CCE2 of (c) SST (d) pH and (e) pCO_2 . Observations are shown in color, while the model simulation results are shown as a black line. Mean bias (MB) and simulated standard deviation normalized to observed standard deviation (σ_n) are given in top left corners for each variable. The black contour in (a) denotes the area of the CCS up to 750 km offshore and is plotted on top of every tenth grid lines of ROMS-BEC grid.

variability of pH and pCO_2 matches the observed variability (Figure 3b), especially at the CCE2 mooring site off Point Conception (Figures 3d and 3e). Yet, the amplitude of the daily variability of surface pH and pCO_2 is underestimated at the three coastal stations on average by -0.0294 pH unit and $-18.0 \mu\text{atm}$, respectively, while these two properties are overestimated at station Papa by 0.0038 pH unit and $8.2 \mu\text{atm}$, respectively. The rudimentary treatment of river inputs in our model (climatological freshwater and no inputs by carbon and alkalinity) likely explains the poor performance of our model at the Cha'ba station, located near the Columbia River plume region (Figures 3a and 3b).

In summary, the evaluation of the model simulated mean state and variability of physical and carbonate chemistry parameters indicates an overall accurate representation of the key variables and processes in the northeast Pacific and CCS in our model. Especially important is that the amplitudes of the observed variabilities in SST, pH, and pCO_2 are well-captured by the model, thus giving us confidence to analyze the occurrence of extreme events on timescales ranging from days to months.

2.5. Definition of Lagrangian Ocean pH-Aragonite Extremes (OAX)

We define a Lagrangian ocean acidification extreme event (OAX) as a spatiotemporal coherent ensemble of locally rare and low pH and Ω_A conditions, relative to the conditions that occur from 1984 to 2019 (Figure 4).

Extreme conditions are defined using a combined criterion requiring both pH and Ω_A to fall below their respective local 1st percentile (Figure 4b), that is, we are using a relative threshold approach. The 1st percentiles are calculated at each grid-cell based on the distribution of the local daily data from 1984 to 2019, that is, we are using a fixed baseline.

To detect OAXs in the upper 150 m of the northeast Pacific (20° – 62°N ; 105° – 155°W), we first identify all grid-cells with extreme conditions by applying the combined pH- Ω_A first percentile criterion. In a second step, we connect all neighboring identified extreme grid-cells that share either an edge or a corner in space and in time on daily time steps (Python `ndimage.label()` [Weaver, 1985]). This methodology allows for the tracking of extreme conditions in a Lagrangian manner, as they propagate in space and time (Figure 4a). This step implies that two initially spatially separated extreme volumes that merge during their lifetime end up forming a single

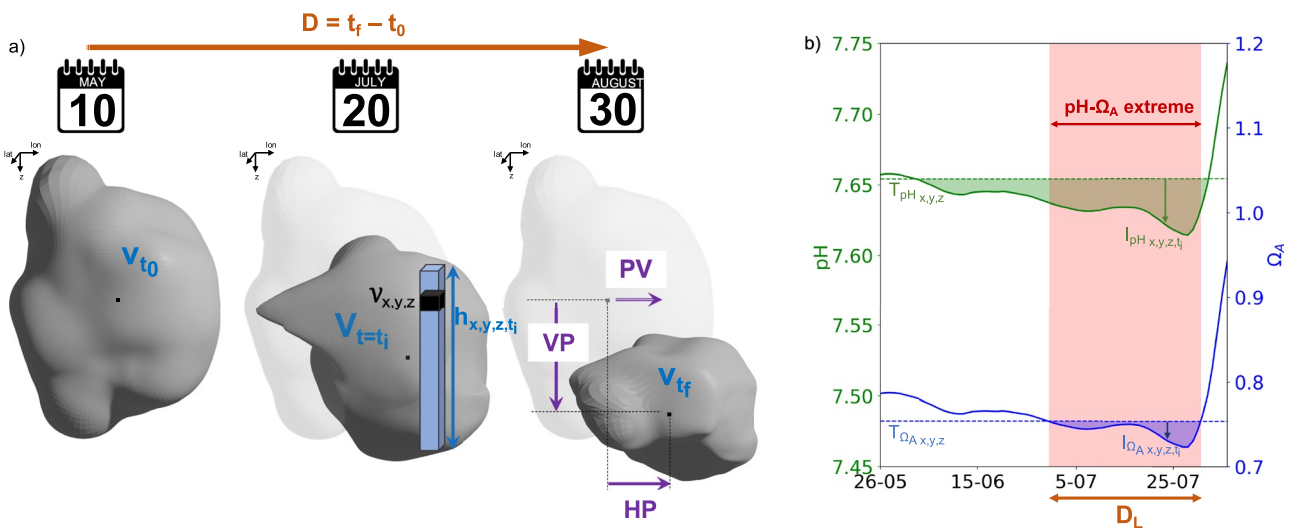


Figure 4. (a) Schematic space-time evolution of an OAX event from its initiation at time t_0 to its waning at time t_f . (b) Time series of pH and Ω_A conditions at a fixed location that the event is passing through. Indicated in both panels are a few characteristics used to diagnose the properties of each event. D , duration; V , volume; h , vertical extent; VP , vertical propagation; PV , propagation velocity; D_L , local duration, that is, of an event at a given fixed location; I , intensity. See Table 1 for detailed explanations.

OAX. Similarly, if several spatially independent volumes of extreme grid-cells originate from a single event in the previous time step, they all remain part of the previous event and form one single OAX. We then discard in an additional step all those events that do not occur, at any time of their lifetime, within the upper 100 m of the water column. This led to a 22% reduction of the number of events. Finally, we discard all OAXs that last less than 5 days, following the general recommendation established for marine heat waves by Hobday et al. (2016). Additional technical details of this detection are given in Text S1 and Figure S6 in Supporting Information S1, together with a list of input requirements and available outputs in Tables S3 and S4 in Supporting Information S1.

The use of a combined pH- Ω_A metric is an example of a multi-variable metric that allows for the quantification of an extreme that (a) affects a range of marine taxa that are either sensitive to one or multiple carbonate chemistry variables (either pH or Ω_A), (b) may be suitable for the quantification of impacts on species where different variables have been shown to affect different life stages, or for (c) species where the lead driver cannot be reliably identified. It is of particular relevance for the ubiquitous calcifying pteropods found in the CCS, by selecting conditions that may be detrimental to pteropod populations across life stages, with pteropod eggs being negatively affected by low pH, and adults by low Ω_A . To acknowledge that extreme metrics based on a single carbonate chemistry variable may be equally or even more relevant for other marine ecosystem constituents, we assess the robustness of our results to the choice of the target variable, as well as the selection of the threshold value in Section 3.5. Note that given our use of a relative threshold, the identified extremes and their spatiotemporal distribution remain unchanged whether one uses pH or $[H^+]$ as the variable of choice. We further assess the overlap between the grid-cells extreme with regard to a single metric and to the combined pH- Ω_A metric in Section 3.5. The sensitivity of the results to a change in the minimum duration of an event is also discussed in Section 3.5.

While detecting extremes down to 150 m, we focus our study on those events that extend at least once in their lifetime into the top 100 m of the water column, as this corresponds to the average modeled euphotic zone in the CCS and in the eastern North Pacific. This is where most phytoplankton and zooplankton biomass is found (Buitenhuis et al., 2013), and where pteropod biomass is highest (Bednaršek et al., 2012). Even though vertical migration of many zooplankton species leads to substantial biomass levels also at greater depth (Bednaršek & Ohman, 2015; Mackas et al., 2005), the highest biomass levels still tend to occur in the top 100 m. For example, pteropod carbon biomass observations in the eastern North Pacific from Bednaršek et al. (2012) reveal that 92% of the total depth-integrated biomass is found in the top 100 m. This goes in hand with the mean and 90th percentile biomass decreasing by one order of magnitude between the upper 100 m depth and below (Figure S7 in Supporting Information S1). By detecting extremes down to 150 m, while focusing only on those events that

Table 1
Definition of Features to Characterize OAXs

Name	Definition	Unit
a) Temporal metrics		
Duration (D)	Lifetime of an ensemble of extreme conditions classified to belong to the same spatiotemporally coherent event	days
Local duration ^a (D_L)	Maximum grid-cell based duration within an event	days
b) Size metrics		
Daily volume (V)	Mean volume of an event over its lifetime $V = \frac{\int_t v_t dt}{D}$ with v_t the total volume of an event at day t	km^3
Vertical extent ^a (\bar{h})	Area weighted average occupation of the upper 150 m of water column by an event	m
c) Intensity-based metrics		
Severity ($S_{\text{pH}}, S_{\Omega_A}$)	Cumulative volume weighted intensity in time and space for pH and Ω_A separately $S = \int_t \int_v (T_{(x, y, z)} - \text{VAR}_{(x, y, z, t)}) dv dt$ with $T_{(x, y, z)}$ the grid-cell threshold, $\text{VAR}_{(x, y, z, t)}$ the pH or Ω_A value at a given grid-cell at a given time and v the grid-cell volume	$\text{km}^3 \text{ d}$
Intensity ($I_{\text{pH}}^a, I_{\Omega_A}^a$)	Volume weighted average intensity: $I = S / \int_t v_t dt$	unitless
VAR (pH, Ω_A)	Volume weighted average pH or Ω_A	unitless
d) Propagation metrics		
Horizontal propagation ^a (HP)	Horizontal distance between the volume weighted center of gravity of an event at initiation and ending	km
Vertical propagation ^a (VP)	Vertical distance between the volume weighted center of gravity of an event at initiation and ending	m
Propagation velocity ^a (PV)	Horizontal velocity of an event: $PS = HP/D$	km d^{-1}

^aFeatures used as input metrics for the clustering of the OAXs.

occupy at least once in their lifetime the biomass-rich upper 100 m of the water column, we avoid the artificial cropping of OAXs at 100 m depth.

2.6. Extreme Event Metrics

The metrics defined to characterize the extreme events need to account for the complexity of the space-time structure of the OAXs emerging from our Lagrangian approach. To quantify the duration, size, intensity, and propagation of each detected extreme event we derive 10 event characteristics (Tables 1a–1d, Figures 4a and 4b).

Core properties of an extreme are its duration and intensity (Gruber et al., 2021; Hauri, Gruber, McDonnell, et al., 2013). Here, the duration of an event, D , refers to the lifetime of the spatiotemporally coherent ensemble of extreme grid-cells that constitute the same event, that is, the time difference from the first occurrence of an event to its last. In addition, we also quantify the local duration of an event, D_L , by diagnosing its maximum duration at one single location (Table 1a). We quantify the extent of an OAX both by its mean volume and its mean vertical extent over its lifetime. The vertical extent is thereby defined as the area weighted average occupation of the upper 150 m of the water column by an extreme over its lifetime (Table 1b). The intensity of an extreme, that is, the difference between the conditions during the extreme and the threshold, is here extended to the space-time dimension of an OAX by using the volume weighted average intensity (Table 1c). We quantify the severity of an event as the cumulative volume weighted intensity in time and space (Table 1c). Both features are calculated for pH and Ω_A separately. We also quantify the volume weighted mean pH and Ω_A within an event (Table 1c).

Finally, we quantify the spatial dynamics of an event through its horizontal and vertical propagation distances and its propagation velocity (Table 1d). The two former features quantify the spatial displacement of an extreme over its lifetime both horizontally and vertically without accounting for any meandering between the initial and the final location of the volume weighted center of gravity of the event. The latter is a measure of the speed at which the extreme is moving horizontally, simply defined by the ratio of the horizontal propagation distance by the duration (Table 1d).

2.7. Clustering of OAXs

We use a clustering analysis to group together OAXs with similar characteristics. We select the input for the clustering of OAXs among all event features defined in Table 1. We first compute the pairwise Spearman's ranked correlations between features (Table S4 in Supporting Information S1). Only one feature from each group of highly correlated ($|r| \geq 0.7$) features is then kept as input for the clustering. Since five features are highly correlated (Table S4 in Supporting Information S1), eight out of the 13 features are retained for the analysis, that is, local duration, vertical extent, pH intensity, Ω_A intensity, Ω_A , horizontal and vertical propagation distances, and propagation velocity. All retained features have pairwise correlations below 0.7 ($|r| < 0.7$). To increase the robustness of the clustering against the choice of input variables, we perform a principal component analysis on the eight selected features. The clustering is then done on the three principal components that have an eigenvalue above 1 (Kaiser's rule; Wilks, 2011). We use a Python K-means algorithm (Pedregosa et al., 2011) to split the detected events into three clusters based on the Silhouette (Rousseeuw, 1987) and Calinski-Harabasz (Calinski & Harabasz, 1974) scores together with the Elbow method on the within-cluster sum of squares (Figure S8 in Supporting Information S1). The robustness of the clusters to the removal and substitution of input variables and to the loss of 5%, 10%, 15%, and 20% of the events have been quantified using the Kappa index of agreement (Cohen, 1960; Landis & Koch, 1977; Table S5 in Supporting Information S1). Lowering the number of input variables from eight ($|r| < 0.7$) to five ($|r| < 0.6$) results in a Kappa index of 0.77, attesting the robustness of the clusters. Furthermore, the index remains above 0.89 when substituting input variables with correlated features and above 0.98 when omitting 5%–20% of the extremes, which indicates strong stability of our clusters (Table S5 in Supporting Information S1).

2.8. Assessment of Drivers

We will analyze the role of two potential drivers for the identified OAXs within each cluster: Upwelling and mesoscale processes, especially eddies. For the former, we will use the Biologically Effective Upwelling Transport Index (BEUTI; Jacox et al., 2018) and for the latter the Okubo-Weiss (OW) parameter (Chang & Oey, 2014; Davis & Di Lorenzo, 2015; Okubo, 1970; Weiss, 1991). The BEUTI quantifies the efficiency of the coastal upwelling (Jacox et al., 2018). By multiplying the vertical transport and the nitrate concentration at the bottom of the mixed layer depth, the BEUTI accounts for both physical vertical transport and composition of the water transported. We calculate the Spearman rank correlation between the monthly occurrence time series of extremes in each cluster and the 31°N to 47°N meridionally averaged BEUTI from January 1988 to January 2019 (Jacox et al., 2018), in order to disentangle events that co-occur with strong upwelling and thus might be initiated by upwelling. The OW parameter quantifies the relative importance between strain and relative vorticity in a grid-cell (Equation 1). A negative OW value depicts a region where the vorticity is larger than the strain and is often used as criterion to define mesoscale eddies (Davis & Di Lorenzo, 2015; Kurian et al., 2011). First, the OW parameter is computed for every grid-cell belonging to an extreme event. Then, we define an OAX to be eddy-driven when more than 70% of all grid-cells belonging to the OAX over its lifetime present an $OW < 0$.

$$OW = S_n^2 + S_s^2 - \zeta^2 = \left(\frac{\partial u}{\partial x} - \frac{\partial v}{\partial y} \right)^2 + \left(\frac{\partial v}{\partial x} + \frac{\partial u}{\partial y} \right)^2 - \left(\frac{\partial v}{\partial x} - \frac{\partial u}{\partial y} \right)^2, \quad (1)$$

where S_n and S_s are the normal and shear components of the strain and ζ the relative vorticity.

We further identify the polarity of eddy-driven OAXs by using the sign of the relative vorticity of the $OW < 0$ grid-cells (Kurian et al., 2011). When more than 80% of the $OW < 0$ grid-cells of an event have a positive vorticity, we associate the extreme with a cyclonic eddy.

In addition to the assessment of physical drivers, we estimate the relative contribution of physics and local biological processes, by comparing a density-predicted Ω_A anomaly to the modeled Ω_A anomaly in OAXs. Our methodology is based on the assumption that a change in density translates into a change in Ω_A due to changes in chemical and biological properties of the water inherent to the heaving of isopycnals. The high correlation between climatological Ω_A and in situ density (Spearman's $r = -0.94$) supports this assumption. The difference between density-predicted and modeled Ω_A anomaly in OAXs is then assumed to result from local and instantaneous changes in biological production/respiration, neglecting nonlinear effects of local mixing. We compute the density-predicted Ω_A in OAXs by fitting a quadratic function to the annual climatological Ω_A and in situ density

in the upper 300 m of the CCS, spatially averaging both fields within $1^\circ \times 1^\circ \times 20$ m bins, and by applying this fit to the average density within each OAX. We exclude regions where the quadratic fit differs by more than 0.6 Ω_A unit between modeled and density-predicted climatological Ω_A , that is, the Columbia river plume region (Figure S9 in Supporting Information S1).

2.9. Sensitivity Cases

We evaluate the sensitivity of our results with regard to the key decisions involved in the definition of OAX, that is, (a) to the choice of percentile and duration thresholds, (b) to the choice of the number of variables to define an extreme, that is, single vs. dual variable criterion, and (c) to the choice of baseline (moving or fixed). We compare the number of detected extreme events, their spatial distribution, and the distribution and range of their characteristics between the main detection (Ref) and seven sensitivity cases, that is,

Ref. Extreme conditions occur when both pH and Ω_A simultaneously fall below their respective local 1st percentile. First percentiles are calculated at each grid-cell over temporally aggregated daily data from 1984 to 2019. An event lasts a minimum of 5 days.

(a)

0.2th Extreme conditions occur when both pH and Ω_A fall below their respective local 0.2th percentile.

0.1th Extreme conditions occur when both pH and Ω_A fall below their respective local 0.1th percentile.

7 days Extreme conditions occur when both pH and Ω_A fall below their respective local 1st percentile but the minimum duration of an event is set to 7 days instead of five.

10 days Extreme conditions occur when both pH and Ω_A fall below their respective local 1st percentile but the minimum duration of an event is set to 10 days instead of five.

(b)

pH only Extreme conditions occur when the pH falls below its local 1st percentile, that is, a one in a hundred days event, regardless of the Ω_A .

Ω_A only Extreme conditions occur when the Ω_A falls below its local first percentile, that is, a one in a hundred days event, regardless of the pH.

(c)

Moving baseline Both pH and Ω_A thresholds decrease over time following the linear trend at each grid-cell of pH and Ω_A respectively.

We then evaluate the robustness of the clusters by comparing the percentage contribution of events to each cluster between the main detection and each of the sensitivity cases. We further assess how different definitions of OA extremes affect the drivers analysis. To this end, we compute for each cluster the mean L1 norm difference (and associated standard deviation) between the correlation of the monthly number of OAXs with BEUTI found for the main detection and for each sensitivity case (Equation 2). We do the same for the percentage of OAXs associated with eddies.

$$\overline{\Delta M_{L1}} = \frac{1}{7} \sum_{n=1}^7 |M_{\text{Ref}} - M_n|, \quad (2)$$

where M is the metric being evaluated, that is, the correlation of the monthly number of OAXs with BEUTI or the percentage of OAXs associated with eddies, and n each of the seven sensitivity cases.

3. Results

3.1. Spatiotemporal Distribution and Characteristics

Overall, we detected in our analysis region (20° – 62° N; 105° – 155° W) between 1984 and 2019 a total of 22,121 OAXs, that is, Lagrangian extreme events. These detected OAXs vary strongly across the depth and between regions and seasons. We visualize the spatial distribution and characteristics of Lagrangian events by projecting

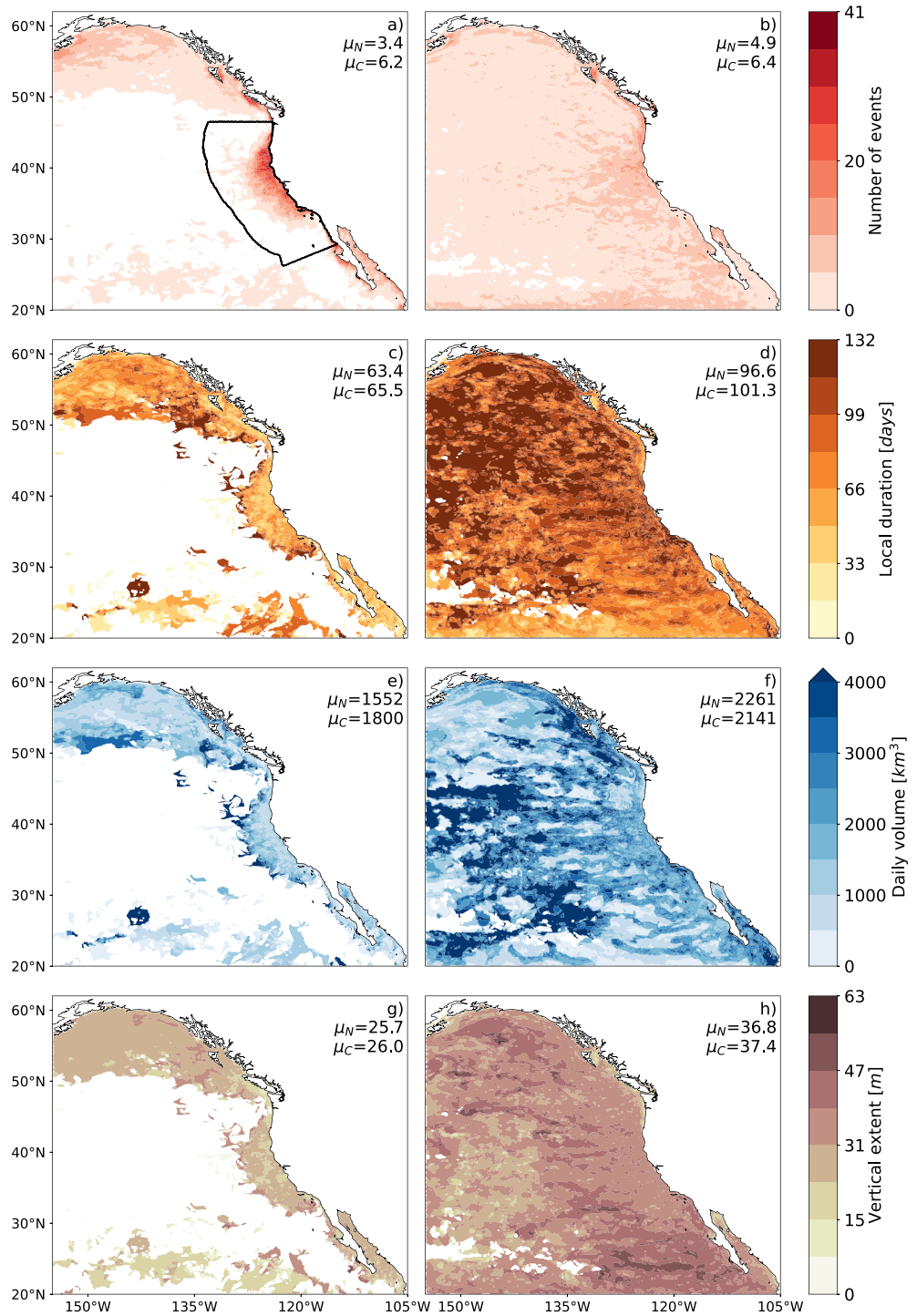


Figure 5. Projection of the characteristics of Lagrangian extreme events, that is, OAXs, onto maps. Shown are metrics determined from the events that pass by a given location (left) at the surface and (right) at 100 m depth. (a and b) Number of events, (c and d) mean local duration (D_L), (e and f) mean daily volume (V), (g and h) mean vertical extent (\bar{h}). The black contour in (a) denotes the area of the California current system up to 750 km offshore. Spatial average of each metric is given for the entire domain (μ_N) and for the California current system (CCS; μ_C).

them onto maps at two different depths, that is, surface and 100 m depth (Figure 5). From 1984 to 2019, the surface experienced, on average, 3.4 events at any location, vs. 4.9 at a depth of 100 m (Figures 5a and 5b). Over the 36 yr of the assessed simulation, this corresponds to roughly one event per 11 and 7 yr, respectively. The

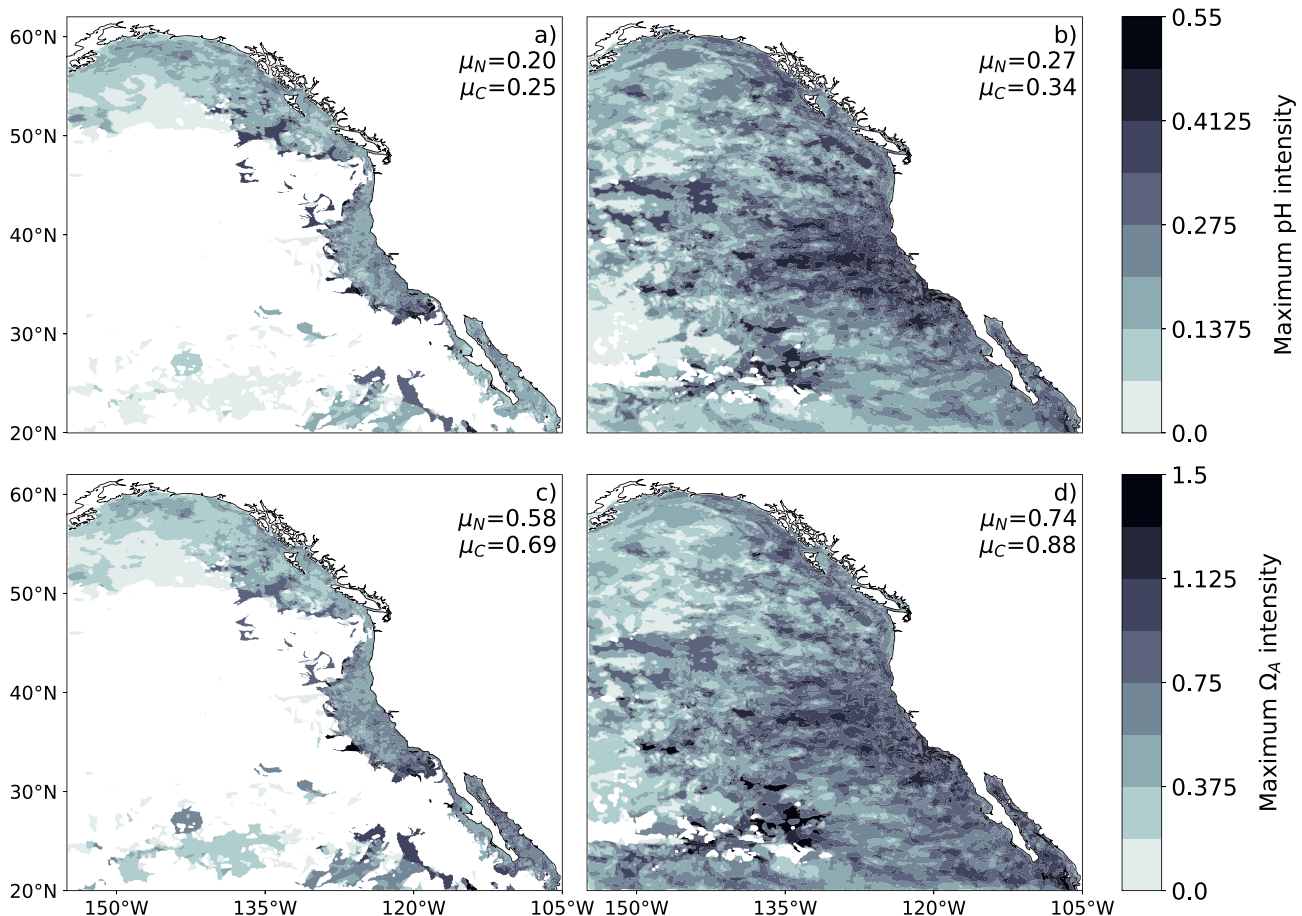


Figure 6. Same as Figure 5 for intensity metrics, that is, the mean maximum (a and b) pH and (c and d) Ω_A intensities reached in events that pass by a given location (left) at the surface and (right) at 100 m depth.

spatial distribution differs substantially between the two depths. At the surface, the number of OAXs exhibits a strong spatial gradient with high numbers in the nearshore central CCS with up to 41 events at a given location (~ 1 event per year) and very few to no events in most of the offshore areas. Overall, nearly twice the number of events occur at any location in the CCS compared to the entire northeast Pacific (Figures 5a and 5b). At 100 m, the events are much more evenly distributed, with most of the domain having experienced at least one pH- Ω_A event between 1984 and 2019. Still, the CCS region harbors 30% more extremes compared to the rest. The highest numbers are found in a corridor around Cape Mendocino, with values as high as 26 events, that is, approaching about one event per year. OAXs are initiated all-year round but they are more frequent from May through July (Figure S10 in Supporting Information S1). In the CCS, the seasonality is more pronounced with 42% of the events starting during May–July and 57% from March to July, when most of the CCS experiences upwelling conditions (Checkley & Barth, 2009; García-Reyes & Largier, 2010).

The durations, volumes, vertical extents, severities, and propagations of the detected OAXs range across a wide spectrum, although with distinct differences between the surface and 100 m. Events passing at 100 m depth tend to be larger, extend vertically more, last locally longer, and be more intense than surface events (Figures 5c–5h, Figure 6).

Locally, and irrespective of depth, the OAXs last from 1 day to more than 4 months (Table 2a). From the Lagrangian, that is, OAX following, perspective their duration ranges from 5 days—the imposed lower bound—to several years. The extreme events with the longest duration (local or total) initiate in the CCS (Table 2a). Over the entire northeast Pacific domain surface events last, on average, ~ 63 days, while the number is 1.5 times higher for events passing at 100 m (Figures 5c and 5d). This difference across depths also applies for the CCS (Figures 5c and 5d).

Table 2

Summary of the Characteristics of the Detected OAXs in the Entire Northeast Pacific and for Those Originating in the California Current System Only, i.e., Those Affecting at Least One Grid-Cell of the CCS on Their Initiation Day

	Northeast Pacific			Originating in CCS only		
	Median	IDR	Max	Median	IDR	Max
a) Temporal metrics						
Duration [days]	9	36	2,989	9	31	2,480
Local duration [days]	6	18	132	5	13	132
b) Size metrics						
Daily volume [km ³]	3.1	28.4	8,393	2.1	18.9	8,393
Vertical extent [m]	9.5	20.2	70.2	10.1	17.8	63.6
c) Intensity-based metrics						
Severity pH [km ³ d]	0.2	11.4	438,331	0.2	9.7	438,331
Severity Ω_A [km ³ d]	0.7	37.4	1,420,570	0.6	31.9	1,420,570
Intensity pH	0.010	0.025	0.091	0.013	0.026	0.091
Maximum pH intensity	0.026	0.087	0.532	0.042	0.106	0.532
Intensity Ω_A	0.027	0.083	0.451	0.036	0.090	0.248
Maximum Ω_A intensity	0.075	0.277	1.634	0.113	0.331	1.420
pH	7.883	0.360	7.462 ^a	7.809	0.387	7.506 ^a
Mean pH in top 150 m ^b	8.032			7.989		
Ω_A	1.34	1.36	0.31 ^a	1.18	1.08	0.31 ^a
Mean Ω_A in top 150 m ^b	2.583			2.093		
d) Propagation metrics						
Horizontal propagation [km]	25	108	3,214	31	117	3,214
Vertical propagation ^c [m]	-2	28	-140 ^a	-4	33	-140 ^a
Propagation velocity [km d ⁻¹]	2.3	6.1	33.0	3.0	7.1	26.3

Note. The median, interdecile range (IDR), and maximum (minimum for pH, Ω_A , and vertical propagation) values are given for each characteristics.

^aMinimum value given instead of maximum value. ^bWeighted mean values over the entire study area (left) and the CCS (right). ^cA negative vertical propagation denotes a deepening of the OAX along its lifetime.

The volume of the detected OAXs ranges from less than a cubic kilometer—close to the lower limit given our grid resolution—to more than 8,000 km³ (Table 2b). Averaged over the northeast Pacific, a typical OAX event has a volume of 1,552 km³ if it passes at the surface and 2,261 km³ for those passing at 100 m (Figures 5e and 5f). Our detected OAXs occupy, on average, 0.35% of the volume of the upper 100 m of the entire northeast Pacific. Although the CCS (black line Figure 3) only represents 14% of the total volume of the domain, events originating in this region account for about half of the total extreme volume.

The local mean vertical extent varies by one order of magnitude, that is, from 1 to 70 m (Table 2b), but the identified OAXs tend to be relatively compressed in the vertical, with a median vertical extent of 9.5 m. Across the full East Pacific, the mean vertical extent amounts to ~26 m at the surface and ~37 m at 100 m. These differences hold also for the OAXs that originate in the CCS (Figures 5g and 5h). Thus, while OAXs occupy large volumes, their small vertical extent implies that these extremes tend to be relatively thin sheets that extend horizontally over areas of typically 70,000 km², that is, a sixth of the surface area of the California state.

As is the case for all metrics, the intensity, severity and absolute pH, and Ω_A levels vary among the detected extremes. pH and Ω_A intensities in the detected events range up to 0.091 pH ([H⁺] intensity of 6.16 nmol L⁻¹) and up to 0.45 Ω_A units, respectively (Table 2c). Locally, pH and Ω_A intensities in the extremes reach 0.532 pH ([H⁺] intensity of 35.39 nmol L⁻¹) and 1.634 Ω_A units. Averaged over the northeast Pacific, a typical OAX event reaches a maximum intensity of 0.20 pH ([H⁺] intensity of 9.24 nmol L⁻¹) and 0.58 Ω_A units if it passes at the surface and 0.27 pH ([H⁺] intensity of 13.50 nmol L⁻¹) and 0.74 Ω_A units for those passing at 100 m (Figure 6 and Figure S11 in Supporting

Information S1). The most severe event initiates in the CCS (Table 2c). The extremes originating in the CCS tend to be more intense, with both higher median pH ($[H^+]$) and Ω_A intensities and lower median pH and Ω_A levels (Figure 6 and Figure S11 in Supporting Information S1, Table 2c). The mean Ω_A within an OAX can go down to strongly undersaturated levels of 0.3. This is seven times lower than the mean Ω_A in the top 150 m (Table 2c).

Last but not least, there are differences in terms of horizontal and vertical propagation of the detected OAXs. While half of the events propagate less than 25 km horizontally, some extremes propagate as far as 3,200 km (Table 2d). OAXs can deepen or shoal by more than a 100 m in the vertical over their lifetime. Their propagation speed ranges up to 33 km d⁻¹ with a median value of 2.3 km d⁻¹, similar to the propagation speed of mesoscale eddies at this latitude (Nagai et al., 2015). The events originating in the CCS propagate 28% faster, on average, than events from the entire northeast Pacific. They also propagate over distances 16% larger, on average, depicting the strong dynamics of the system.

The large variety of OAXs events in the northeast Pacific in terms of spatiotemporal occurrence, size, strength, and propagation arises from the interplay of complex physical and biogeochemical processes. But it also suggests that different combinations of processes are at play, leading to different classes of extremes. In order to check for the existence of such classes, we cluster the events, and then attempt to disentangle the different types of events and their associated drivers. We thereby limit our analyses to the OAXs originating in the CCS up to 750 km off the coast, owing to the higher number of events in this region as well as their higher severity in comparison to the rest of the study area.

3.2. Cluster Analysis

Across the entire northeast Pacific, the K-means based cluster analysis identifies three main categories of OAX (Section 2.7) with 777, 4,589, and 16,755 events, respectively. We refer to them as (a) large, long, and propagating (LLP), (b) intense, shallow, and coastal (ISC), and (c) small mid-depth (SMD) events (Figure 7a). The clusters are well separated, with them differing statistically significantly for each of the eight input variables ($p < 0.05$) based on a Kruskal-Wallis (Kruskal & Wallis, 1952).

In the following, we focus only on those events that originate in the CCS. This choice is based on these events dominating the northeast Pacific in terms of number, volume, and strength of OAX. This lowers the number of events in each cluster to 223, 2,113, and 4,526 for the LLP, ISC, and SMD clusters, respectively (6,862 events in total). The LLP and ISC events originating in the CCS account for 49% and 30% of the total extreme volume of all LLP and ISC OAXs respectively. The extreme volume of the third cluster, SMD, is more evenly spread over the whole domain with only 13% corresponding to events starting in the CCS.

OAXs that belong to the LLP cluster stand out from the other extremes in many regards. They last longer, occupy larger volumes, and propagate much further than the events in the ISC and SMD clusters (Figure 7b). With a median duration of 226 days, LLP OAXs last 20 times longer than those in the other clusters. The median stay at a given location of LLP events is 56 days, that is, 10 times that of the ISC and SMD events (Figure 8d). LLP events can occupy as much as 8,393 km³, with a median volume of 111 km³. In the vertical, these events extend up to 64 m on average over their lifetime, with a median vertical extent of 36 m (Figure 8a). LLP extremes together represent more than 97% of the cumulative severity of all events both in pH and Ω_A , while they account for only 3.2% of the total number of events (Figure 7c). This is mainly a result of their large volumes. In addition to their severity, half of the LLP events harbor mean Ω_A conditions below 1 (Figure 7c), meaning that most of their volume is undersaturated. 51% (37%) of the cumulative pH (Ω_A) severity of all LLP OAXs is associated with Ω_A undersaturated waters. In these events, Ω_A drops as low as 0.64. OAXs in the LLP cluster propagate over large distances, up to 3,200 km with a median horizontal propagation distance of 366 km, unlike extremes from the ISC and SMD clusters that propagate respectively 6 and 16 times less based on their median (Figure 8b). The LLP events occur everywhere in the CCS (Figure 7a) but tend to have their center of gravity further offshore than the other two types of events. They tend to extend throughout the whole water column close to the shore and to deepen when propagating offshore, as indicated by a median deepening of 60 m over their lifetime (Figure 8f). LLP events form quite uniformly during the year, with a slight increase in occurrence from March through July (Figure 7b).

OAXs that belong to the ISC cluster are characterized by higher intensities and stronger propagation velocities than the other two clusters (Figures 8c, 8g and 8h). ISC extremes have medium duration, volume, and vertical extent (Figure 7b). They last no more than 176 days, with a median of 9 days and a median stay at a given location

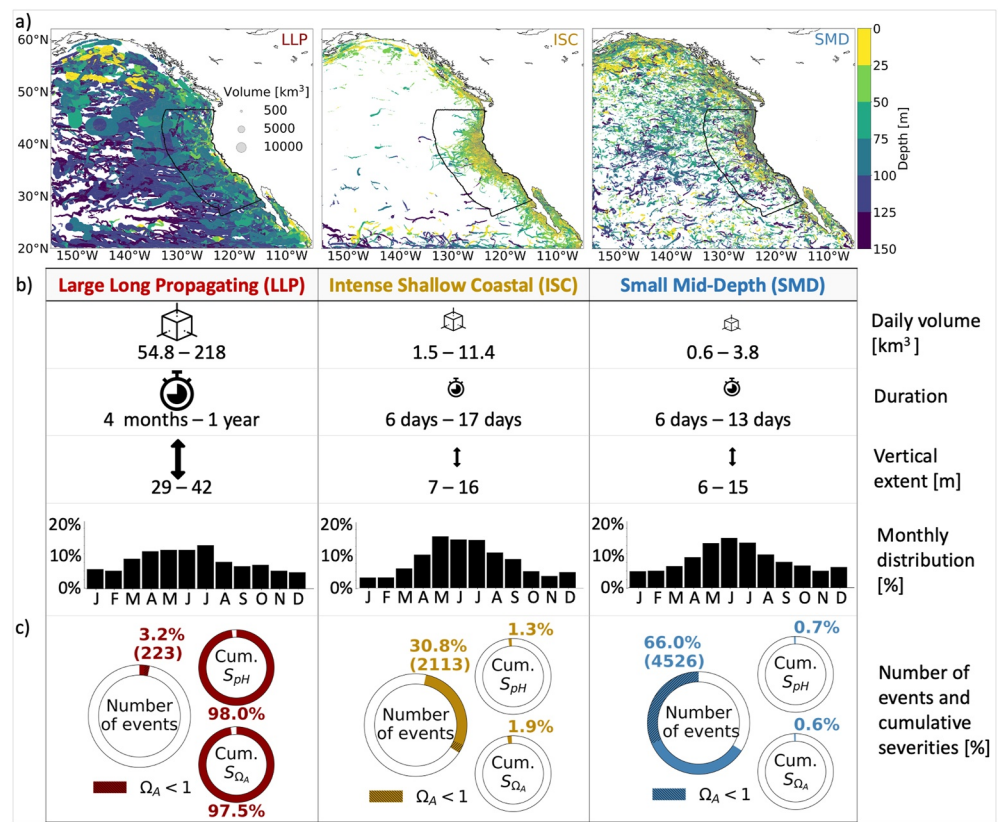


Figure 7. Spatiotemporal extent and distribution of the OAXs within each cluster. (a) Trajectories of the center of gravity of each OAX within a given cluster. The color indicates the mean depth of the extreme at each given day of the trajectory. The dot size scales with the volume of the extreme at each given day. The black line encompasses the focus area for the study, that is, the California current system (CCS) up to 750 km off the coast. (b) For each cluster, the first and third quartiles of volume, duration, and vertical extent from events initiated within the CCS (black contour) are given, as well as their monthly distribution in percentage according to the initiation month (lower bar plots). (c) Distribution of number of events (left) and cumulative severity in pH (top right) and in Ω_A (bottom right) between the three clusters. Hatched sections in the left chart denote the number of events with a mean Ω_A below 1 in each cluster.

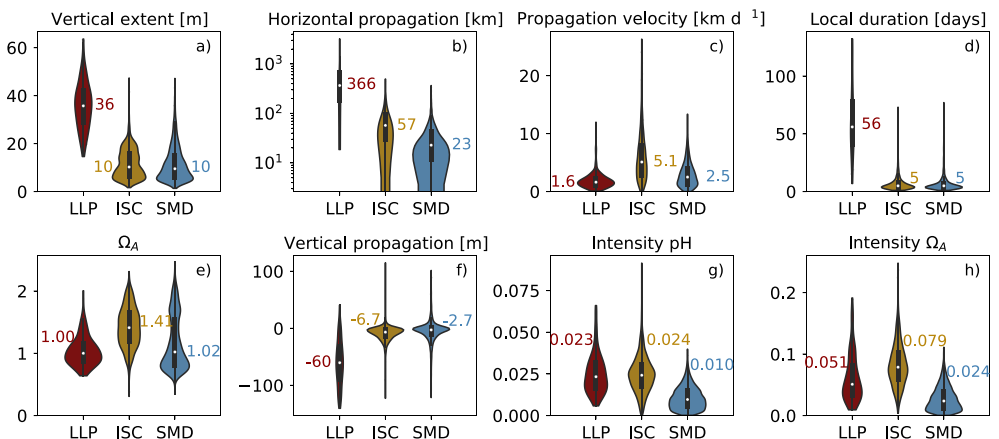


Figure 8. Distribution of the eight features used as input variables for the clustering across the three groups of OAXs for events initiating in the CCS. Medians of each cluster are given.

of 5 days (Figure 8d). They can be as large as 364 km³, but their median volume is relatively small (4 km³). Vertically, they are thin, with an extent of 10 m only (Figure 8a). ISC events stand out for their Ω_A intensity, 55% higher than in the LLP cluster, and thrice as high as in the SMD cluster. While events in ISC have Ω_A intensities up to 0.248, with a median of 0.079, Ω_A intensities in the LLP and SMD clusters only reach 0.191 ($\mu = 0.051$) and 0.111 ($\mu = 0.024$), respectively (Figure 8h). In contrast, while the median pH intensity of ISC cluster is still twice that of the SMD cluster, it is not significantly different from the median pH intensity of the LLP cluster extremes ($p > 0.7$, post hoc Dunn test on CCS OAXs only), that is, 0.023 (Figure 8g). This results in a higher contribution of ISC to the cumulative Ω_A severity (1.9%) compared to pH (1.3%; Figure 7c). The same difference among clusters hold for OAXs [H⁺] intensity (Figure S12 in Supporting Information S1). ISC events also differ in their mean Ω_A state, with a median Ω_A of 1.41 compared to the 1.00 and 1.02 median values of LLP and SMD clusters, respectively (Figure 8e). As a result, only 9% of ISC events harbor undersaturated conditions, a percentage five times lower than in the other two clusters (Figure 7c). Yet a quarter of the cumulative severity of all ISC extremes co-occurs with Ω_A undersaturation conditions. The aragonite saturation state drops as low as 0.3 in the ISC OAXs, that is, 85% lower than the annual mean Ω_A level in the top 150 m of the CCS. Although ISC extremes do not propagate as far as LLP events, they tend to propagate thrice faster (Figure 8), as well as twice faster than SMD events (Figure 8c). ISC extremes have a well-defined spatiotemporal distribution. Eighty eight percent of ISC events have their center of gravity within the upper 40 m of the water column, 96% in the upper 50 m, and 59% within a 100 km coastal band, although they extend further off central CCS (Figure 7a). ISC extremes have a strong seasonality with two thirds of the events starting from April through August.

OAXs that belong to the SMD cluster are the smallest both in terms of volume and vertical extent and propagate the least, with only 5% of SMD OAXs propagating more than 100 km horizontally. They are also the least severe, contributing to only 0.6% of the cumulative severity both in Ω_A and pH (Figure 7c). However, the SMD cluster gathers more than 65% of the total number of the OAXs originating in the CCS. Furthermore, nearly half of these events are undersaturated with respect to aragonite (Figure 7c). Spatially they tend to occur close to the coast, and right at the lower bound of the mixed layer, defined according to the KPP scheme (Large et al., 1994). Similarly, to ISC events, they mostly initiate during spring and summer.

3.3. Spatiotemporal Evolution of OAXs

The three types of OAX evolve differently in time and space. LLP extremes tend to start in the nearshore where they extend throughout the upper 150 m depth (Figure 9). Their vertical extents tend to shrink as they propagate offshore in the form of eddies and filaments. During their lifetimes, LLP extremes often split into isolated volumes of extreme conditions that are no longer spatially connected to the main extreme volume (Figure 9). We still consider them as one event, since these isolated volumes can be traced back in time to a common parent event. As a result, the shape of the extreme morphs constantly, representing overall more a connected series of events rather than a well-defined event. In rare occasions, the residual isolated volumes from an extreme get connected to the onset of a new wave of extreme volumes leading to a few LLP extremes lasting over several years. Also, the ISC events originate in the nearshore CCS, but they are confined to a thin and shallow layer of the water column (Figure 10). As they age, they tend to disconnect from the shore and rapidly become weaker without propagating far offshore. The SMD events occur locally in both the nearshore and the offshore regions, usually below the mixed layer depth. They propagate little and also disappear fast again (Figure 11).

3.4. Multiple Drivers of OAXs in the CCS

The diversity of OAX events emerges from the interaction of physical and biogeochemical processes. The presence of three distinct clusters of events suggest that these interactions follow three distinct sets of storylines. We attempt here to extract these storylines for each of the three clusters, recognizing that the key ingredients are wind-induced coastal upwelling and mesoscale circulation. These two processes are well known to drive most of the natural variability in the carbonate chemistry of the CCS (Hauri et al., 2009; Hauri, Gruber, Vogt, et al., 2013).

The monthly number of OAXs within each of the three clusters correlates positively and significantly (Spearman correlations, $p < 0.05$) with the BEUTI upwelling index (Table 3e), indicating that the strength of upwelling along the U.S. West Coast plays an important role in driving the events that originate in the CCS. At the same

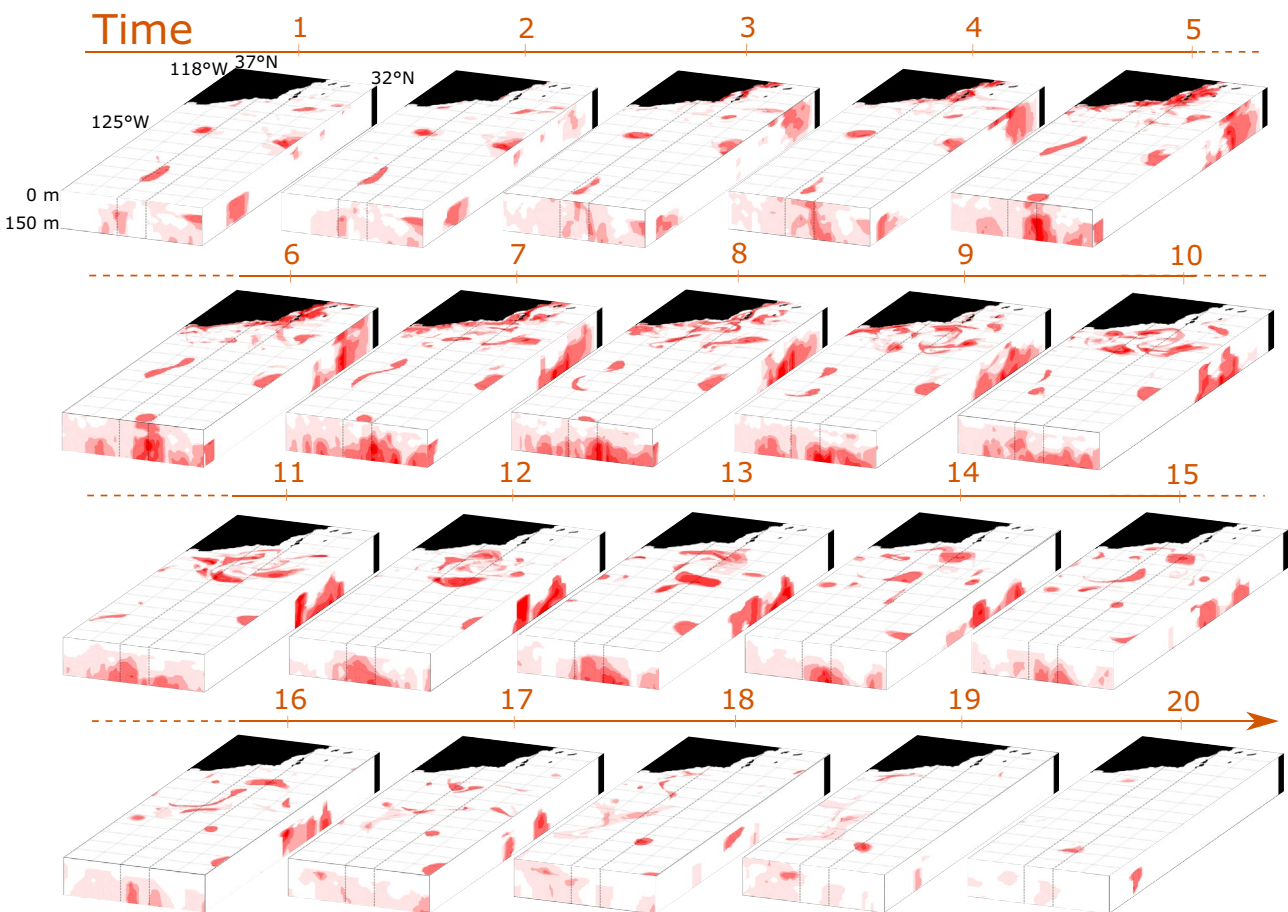


Figure 9. The most severe large, long, and propagating (LLP) originating from the California current system (CCS) starts in the Southern California Bight where it develops into many mesoscale eddies trapping the upwelled waters. When a new upwelling event occurs in the Southern California Bight (1–6), the upwelled waters start to be stirred into filaments propagating further offshore and progressively getting trapped into eddies that merge with the remaining eddies of the extreme (7–12), building up a long extreme event. These eddies continue to propagate the extreme over large distances and periods of time (13–20). The red opacity scales (top map) the vertical occupation in the top 150 m of the water column (longitudinal cross-section), the meridional occupation within the 34° to 35° N latitudinal band (gray dashed lines) and (latitudinal cross-section) the zonal occupation of the extreme. One degree longitude bins are shown by the gray solid lines.

time, at least a third of all events are also associated with mesoscale cyclonic eddies as diagnosed from the OW parameter (Table 3f). The two associations are inversely related across the three clusters. The higher the correlation coefficient with the BEUTI, the smaller the cyclonic eddy association.

The ISC cluster exhibits the strongest correlation between the monthly occurrence of its events and the BEUTI ($r = 0.60$), and the weakest association with eddies (34% of ISC events). Moreover, the ISC events are characterized

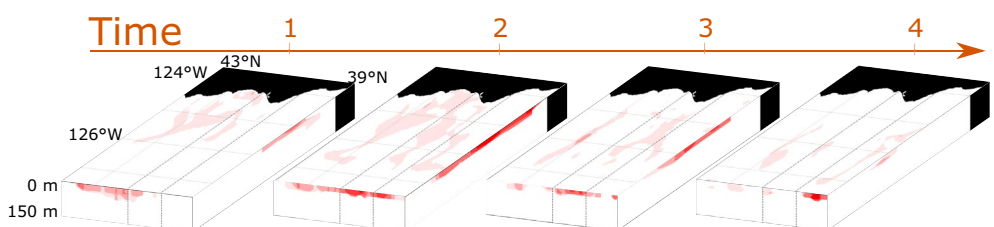


Figure 10. The most severe intense, shallow, and coastal (ISC) originating from the California current system (CCS) starts in the coastal surface waters of the central CCS (1). The extreme expands slightly offshore (2) before it gets disconnected from the coast (3), and rapidly vanishes (4). Note that the longitudinal extent of the top map is thrice smaller as for the large, long, and propagating (LLP) extreme. The meridional occupation is computed within the 40° to 41° N latitudinal band (gray dashed lines).

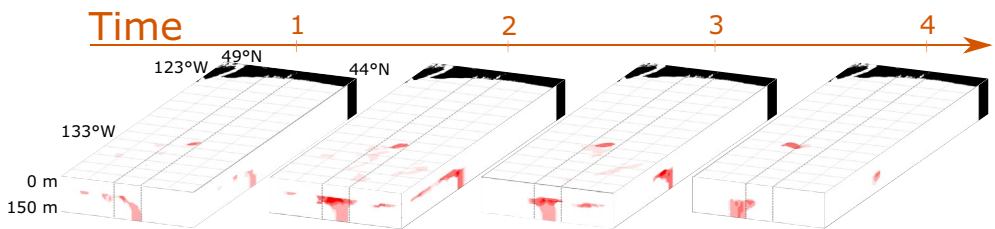


Figure 11. The most severe small and mid-depth (SMD) originating from the California current system (CCS) starts in the offshore subsurface waters (1). It expands slightly at the thermocline edge (2) before it shrinks again (3), and rapidly disappears (4). The meridional occupation is computed within the 46°–47°N latitudinal band (gray dashed lines).

by the coldest temperature and strongest density anomalies of all clusters (Tables 3e–3h). These anomalies together with the high correlation with the coastal upwelling index and their spatial pattern (Figure 7a), indicate that ISC events are directly caused by strong upwelling events that bring subsurface waters with low pH and low Ω_A to the near-surface. The ISC extremes then tend to be entrained into mesoscale filaments (Figure 7a) that can extend several 100 km into the open ocean (Figure 8b). The direct association with filaments is also confirmed by the offshore speed of the ISC events (up to 0.49 ms^{-1} , Figure 8c), which matches the flow velocities of mesoscale filaments ($0.1\text{--}0.5 \text{ ms}^{-1}$, Lovecchio et al., 2018). More than half of the ISC events subduct over their lifetime with mean downward velocity of up to 25 md^{-1} . These negative vertical velocities are reminiscent of those seen in filaments, that is, $5\text{--}10 \text{ md}^{-1}$ (Nagai et al., 2015). As the filaments often spawn mesoscale eddies, some of the ISC cluster events continue their lives as mesoscale eddies. As cyclonic eddies being spawned at the end of a filament can trap the upwelled waters, nearly all eddy associated ISC events occur in cyclonic eddies.

Even though not as high as in the case of the ISC cluster, the substantial correlation of the number of OAX events of the SMD cluster with the BEUTI index ($r = 0.49$, Table 3e) still suggests upwelling events to be important in generating SMD events. This is confirmed also by the substantial negative temperature anomalies and positive density anomalies in those events (Table 3g and 3h). But less than 15% of the SMD events occur within the mixed layer and 42% form outside of the nearshore 100 km, so that the positive correlation with the BEUTI emerges from the general uplifting of the pycnocline with its low pH and Ω_A during upwelling. Cyclonic mesoscale eddies can cause a similar uplifting of the pycnocline, potentially explaining the 40% of SMD cluster events to be associated with cyclonic eddies.

While the LLP OAX events are still significantly positively correlated with the BEUTI ($r = 0.16$, Table 3), their very high association with cyclonic mesoscale eddies (83%) suggests that the latter are the primary mechanisms causing this type of event (Tables 3f–3g). These eddy-induced LLP events initiate all-year round (Figure 7b).

Table 3

Summary of (a–c) Spatiotemporal Distribution, (d–f) Main Regional Oceanic Drivers, and (g, h) Mean Temperature and Density Anomaly of OAXs Originating in the CCS Within Each Cluster

	Large, long, and propagating (LLP)	Intense, shallow, and coastal (ISC)	Small and mid-depth (SMD)
(a) Region	Throughout CCS	Upwelling zone	Throughout CCS
(b) Depth	All water column at initiation; deepen while propagating offshore	Surface top 40 m	Mixed layer depth
(c) Season	All	April–August	April–August
(d) Oceanic processes	Cyclonic eddies	Strong upwelling, filaments trapping	Pycnocline variability and small scale features
(e) Corr ^a with BEUTI	0.16	0.60	0.49
(f) % of eddy events ^b (of those % cyclonic ^c)	83% (99%)	34% (93%)	39% (94%)
(g) Mean temperature anomaly (°C)	-1.50	-2.45	-1.45
(h) Mean density anomaly (kgm ⁻³)	+0.51	+0.67	+0.46

^aSpearman correlation with $p < 0.005$. Computed using monthly occurrence time series of the events and the 31°N–47°N meridionally averaged BEUTI from 1998 to 2019. ^bAn OAX is counted as an eddy event if more than 70% of its grid-cells have a negative OW, i.e., $OW < 0$. ^cAn eddy event is considered as cyclonic if more than 80% of its grid-cells with negative OW have a positive vorticity.

However, their frequency peaks from March through July (Figure 7b) when cyclonic eddies trap upwelled coastal waters with low pH and Ω_A into their core (Amos et al., 2019; Chelton et al., 2011; Chenillat et al., 2016; Kurian et al., 2011; Lovecchio et al., 2018). Many of the LLP events originate from two regions only, that is, the region between Cape Mendocino up to Cape Blanco (39° – 43° N) and the region around Point Conception (33° – 36° N). This holds especially for the long-lived LLP extremes ($D > 180$ days), of which half originate from these two regions alone (24% and 26%, respectively). LLP eddy-driven OAXs move offshore about 480 km on average and up to three thousand kilometers with a poleward deviation (not shown), corresponding to the displacement of the cyclonic eddies of the CCS (Kurian et al., 2011).

In each of the three clusters, physically driven changes are the main contributor of the Ω_A anomaly seen in the OAXs, based on the density-predicted Ω_A approach defined in Section 2.8. Locally increased respiration contributes up to 29% and 35% on average of the lowering of the Ω_A in the SMD and LLP extremes, respectively, while the change in density tends to fully explain the Ω_A anomaly found in ISC extremes (Figure S13 in Supporting Information S1).

3.5. Sensitivity Analysis

Despite the many choices made to define OAXs, their spatial distribution, characteristics and the relative role of upwelling and mesoscale eddies in driving the different group of extremes are robust to several key decisions in the definition. In general, the spatial gradient in OAX occurrence is preserved across all the considered cases (Section 2.9), despite the fact that the total occurrence within the northeast Pacific changes strongly in response to a change in the percentile, minimum duration, baseline or metric used for the definition (Figures S14 and S15 in Supporting Information S1). The number of detected OAXs increases with a weaker threshold while it decreases with more restrictive thresholds (Figure S15a in Supporting Information S1). Changing the minimum duration threshold from 5 to 10 days lowers the number of events by half while doubling their median volume and duration (Figures S15a–S15c in Supporting Information S1). In general, the volume, duration, local duration, and horizontal propagation are sensitive to a change in the minimum duration threshold, while pH and Ω_A intensities are more sensitive to a change from pH- Ω_A extremes to either only pH or only Ω_A extremes (Figure S15 in Supporting Information S1). When detecting extreme events only with regard to Ω_A , the median Ω_A intensity is lowered by half, indicating that the combined criterion selects for stronger acidification extremes. The same applies for pH intensity when only pH extremes are evaluated. Extreme conditions with regard to only pH or Ω_A overlap with those based on the combined pH- Ω_A criterion in 64% (49%) of the cases in the upper 100 m of the CCS (entire domain). The overlap is largest in regions with the highest number of events and intensities, as well as the highest biological productivity (Figures 5a, 5b and 6; Figures S16a and S16b in Supporting Information S1). Patterns deviate mostly in surface offshore areas, associated with low biological productivity (Figures S16a and S16b in Supporting Information S1) during winter-spring (summer) for the single metric Ω_A (pH; Figures S16c and S16d in Supporting Information S1). The distribution of event characteristics is not sensitive to the lowering of the percentile of the threshold to 0.2th and 0.1th (Figures S15b–S15h in Supporting Information S1), but the 0.05% largest, longest, and most propagating OAXs (~11 events) are suppressed, thus lowering the end of the range of the volume, duration, and propagation features by a factor of ten, three, and two respectively (not shown). The use of a fixed or moving baseline does not appear to significantly affect the number of events, their distribution, and their key characteristics, but has a strong impact on the temporal distribution of these events from 1984 to 2019 (not shown).

Using alternative choices for the detection of OAXs leads to very similar clusters in terms of the percentage contribution of events to each cluster. However, with more restrictive definitions, the percentage contribution of events to the LLP cluster increases (Tables S6d–S6g in Supporting Information S1). This results both from a reduction in the size, duration, and horizontal propagation of the largest, longest, and most propagating detected events and the omission of very small, short, and standing events due to stronger thresholds, both shifting in terms of percentage the distribution of events among clusters.

The ranking of cluster-specific correlation coefficients between the number of monthly extreme events and the BEUTI is conservative with regard to the changes in definition. The ISC cluster exhibits the largest correlation with a mean change in correlation of 0.05 ± 0.04 (L1 norm) between the main detection and each of the sensitivity studies. The SMD cluster exhibits the second largest correlation with a mean change of 0.12 ± 0.05 , and the LLP cluster the lowest correlation with a mean change of 0.01 ± 0.01 . However, the results from the detection on

either pH or Ω_A separately constitute an exception in terms of clusters. In each of these two detections, events with characteristics associated with either the ISC or the SMD clusters in the main detection gather into one single cluster. Surface offshore events that do not happen in the pH- Ω_A detection due to the phase difference between the two carbonate variables in the surface offshore area (Kwiatkowski & Orr, 2018; Xue et al., 2021), form the third cluster. In those sensitivity studies, the resulting {ISC + SS} cluster is the most correlated to BEUTI. The LLP cluster stays robust to the switch from double to single-variable detection. The same applies to the percentage of eddy-driven events in each cluster. The mean difference in percentage between results from the standard methodology and those of all our sensitivity tests (L1 norm) is $4.1\% \pm 2.7\%$ for LLP, $3.4\% \pm 2.6\%$ for ISC, and $5.9\% \pm 4.5\%$ for SMD, implying that the LLP cluster largely remains with the highest percentage of eddy-driven extremes in all sensitivity studies.

Although we did not evaluate the sensitivity of the results to a change from relative to absolute thresholds, we found that a large fraction of the severity of our statistical OAXs is associated with Ω_A undersaturated conditions (Section 3.2), bridging the gap between relative and absolute thresholds.

4. Discussion

4.1. Patterns and Characteristics of OAXs

Recognizing that our Lagrangian analysis approach of OA extremes differs fundamentally from the traditionally used Eulerian approach, we still attempt to compare, to the extent possible, our results to those of the previous studies employing an Eulerian approach. Duration and intensity gradients between surface and depth (~ 100 –200 m) found for OAXs match those previously found by Burger et al. (2020) and Hauri, Gruber, McDonnell, et al. (2013). All three studies agree that extremes occurring at depth tend to last longer and to be more intense than events at the surface. However, the intensity and duration of OAXs detected in our work are higher and longer than those of OA extremes reported in previous studies, both at the surface and at depth (Burger et al., 2020; Hauri, Gruber, McDonnell, et al., 2013). Our Ω_A only sensitivity study (Section 3.5), where we replace the dual variable criterion by a criterion on Ω_A only, shows that the dual selection criterion tends to select the strongest events among all those that lie below the Ω_A threshold, increasing the median intensity of OAXs by a factor of two (Figure S15g in Supporting Information S1, Section 3.5). Thus, changing from dual to single variable criterion for defining OAXs brings our results with regard to intensity closer to the findings of Burger et al. (2020) and Hauri, Gruber, McDonnell, et al. (2013), who used a criterion on a single variable only. Also, the Lagrangian approach taken in our work increases the maximum intensity and the local duration of extremes. The Lagrangian approach allows for the connection of extreme grid-cells horizontally and through deeper layers. The maximum intensity and local duration of our OAX correspond to the strongest intensity and the longest local duration among all grid-cells belonging to that OAX, including grid-cells that sit deeper and often carry higher intensities and see longer events. This means that compared to Burger et al. (2020) and Hauri, Gruber, McDonnell, et al. (2013), we report a higher intensity and longer duration in all the grid-cells that were hit by the OAX, but did not locally experience the reported maximum intensity and local duration. In addition to the many differences in definition of OA extremes, the lack of interannually or decadally varying atmospheric forcing in Hauri, Gruber, McDonnell, et al. (2013) likely led to an underestimation of their reported intensities and durations.

4.2. Drivers of OAXs

Mechanistically, the spatial pattern of the formation of ISC events is well supported by what is known about coastal upwelling in the CCS. Specifically, the sites where ISC events occur correspond very well to the places with high climatological mean vertical velocities at the base of the mixed layer during upwelling season from March through August (Jacox et al., 2018). The comparison reveals that across the nearshore CCS, the larger the positive vertical velocity, the more ISC events are being initiated. In particular, the maximum upward transport and offshore Ekman transport occurs around 40°N (Jacox et al., 2018), that is, south of Cape Mendocino, matching the latitude where the number of ISC events peaks and where they extend the furthest offshore (Figure 7a). The fact that ISC extremes are characterized by a strong Ω_A intensity is consistent with the upwelling water being sourced by waters stemming from 150 to 250 m depth (Frischknecht et al., 2018), often undersaturated with respect to aragonite ($\Omega_A < 1$; Fassbender et al., 2011; Feely et al., 2016). However, despite being intense, only 9% of the ISC extreme events are corrosive (Section 3.2). This is in agreement with the finding that most of the

upwelled waters off Cape Blanco and Cape Mendocino, initially undersaturated, see their Ω_A level restored along the upwelling path by biological productivity and gas exchange (Fassbender et al., 2011).

Our finding that LLP OAXs are primarily driven by cyclonic eddies is supported by the spatial match between the sites where they are initiated (Section 3.4) and the sites where most of the cyclonic eddies are being generated, that is, Cape Blanco ($\sim 42^\circ\text{N}$) and Point Conception ($\sim 34^\circ\text{N}$; Kurian et al., 2011). The fact that 99% of the eddy-driven LLP OAXs are associated with cyclonic eddies (Section 3.4) is in agreement with the finding that most of the eddies in the surface CCS are cyclonic eddies (Kurian et al., 2011) and that cyclonic eddies trap coastal waters more efficiently, for longer periods and over longer distances, than anticyclonic eddies (Chenillat et al., 2016; Nagai et al., 2015). The strong occurrence of long-lived ($D > 180$ days) LLP events (Section 3.4) spatially coincides with the strong density of long-lived cyclonic eddies, that is, with a lifetime longer than 180 days, around Cape Mendocino (40°N) in the surface CCS reported by Kurian et al. (2011). Additionally, the relatively weak seasonality in the occurrence of LLP events (Figure 7b) matches the absence of strong seasonal pattern in the number of eddies in the CCS top 100 m (Kurian et al., 2011). Instead, the eddies show an increase in their strength during summer. This may enhance the formation of the most intense LLP OAXs, as they trap the upwelled waters during spring/early summer, when pH and Ω_A are the lowest, and nutrients the highest (Nagai et al., 2015) owing to the seasonal maximum in upwelling. The enhanced productivity will cause more intense respiration in offshore areas later in the year (as seen by Lovecchio et al., 2017 in the Canary current system). This is consistent with our estimated upper bound of biological contribution of 35% to Ω_A anomalies in LLP extremes (Section 3.4). Some winter LLP OAXs may form due to cyclonic eddy-induced pumping that displaces the nutricline upwards at the eddy formation, locally lifting DIC-rich waters to shallower depths (Chenillat, 2015). The persistence of these events may be associated with the trapping of the initial nutricline doming rather than permanent pumping throughout the event lifetime. Indeed, eddy-pumping has been shown to contribute very little to the nutrient supply in cyclonic eddies (Dufois et al., 2016; Lovecchio et al., 2022). A detailed identification of the mechanism involved in the formation of each LLP OAXs would require the tracking of the cyclonic eddies and their biogeochemical state to identify what happens in the eddy prior to the OAX initiation.

In line with Palacios et al. (2004) who found that the CCS offshore thermocline reaches its shallowest depth in spring/summer, we found a peak in SMD events also during this period (Section 3.2). The depth of occurrence as well as the timing of SMD events may be attributed to thermocline oscillations, as well as intense remineralization of organic matter that rains down from upwelling-induced blooms that can reduce pH in the thermocline (Hauri, Gruber, Vogt, et al., 2013).

4.3. Potential Impacts of OAXs on Marine Organisms

By analyzing the temporal evolution and propagation of OA extremes using a Lagrangian perspective, we reflect the duration of exposure of pelagic plankton during OA extremes with more realism than can be achieved using an Eulerian framework (Bednářek et al., 2017). In particular, the Lagrangian framework captures the potential aggravation of biological impact emanating from the fact that marine plankton tends to drift with an extreme, thereby substantially prolonging its exposure to extreme conditions in comparison to for example, a benthic organism that is exposed to this extreme in passing only.

While it is beyond the scope of this work to assess path-dependent organismal responses for specific taxa or physiological functions, our results permit to identify a number of potential impacts of our OAXs on one example taxa toward which our extreme metric was tailored. We use the pteropod *Limacina helicina* as an example, since it is abundant in the CCS, has been well studied, and is known to be negatively impacted by both low pH and low Ω_A (Bednářek et al., 2019, 2014, 2017; Bednářek & Ohman, 2015; Manno et al., 2012, 2016; Mekkes et al., 2021). Furthermore, *L. helicina* mainly occurs within the top 100 m of the water column (Bednářek et al., 2014, 2012; Bednářek & Ohman, 2015).

Bednářek et al. (2014) derived an empirical formula that predicts the proportion of *L. helicina* individuals with severe shell dissolution as a function of the fraction of the CCS top 100 m undersaturated with regard to aragonite (Appendix A, Equation A1). We apply this formula to each OAX with mean conditions of Ω_A below 1. Their vertical extent \bar{h} serves as a proxy for the average percentage of undersaturated waters in the top 100 m when and where each event occurs. However, only the mean Ω_A of the OAX is required to be below 1, which suggestss that part of the OAX vertical extent is associated with supersaturated conditions. The percentages given below

are thus the upper bound of the proportion of individuals that might experience severe shell dissolution. We find that on average 41% of individuals present in LLP OAXs with corrosive conditions will undergo severe shell dissolution (Type II or III dissolution, Bednaršek et al., 2014), while this value drops to 22% and 24% for ISC and SMD OAXs, respectively.

Additionally, Bednaršek et al. (2017) described a linear relation between *L. helicina* survival probability and its exposure history (“undersaturation-days”) to low Ω_A environmental conditions, accounting for the number of undersaturated days over a given past period and the intensity of the undersaturation relative to a threshold of $\Omega_A = 1$ (Appendix A, Equation A2). We computed for each cluster the mean “undersaturation-days” metric (Bednaršek et al., 2017) based on the duration and the mean intensity relative to $\Omega_A = 1$ of OAXs in undersaturated mean conditions. We computed a mean “undersaturation-days” value of 2.0 and 2.8 days in clusters ISC and SMD, respectively. Following Bednaršek et al. (2017), if an *L. helicina* individual would happen to be trapped into one of the ISC or SMD extreme event, its chance of survival would be less than 50%. This survival probability gets even lower for LLP events that have 36 days of “undersaturation-days” on average (median of 22 days). However, this can no longer be translated into a biological effect, since the maximum “undersaturation-days” reported by Bednaršek et al. (2017) is about six. This is due to the fact that Bednaršek et al. (2017) limit the time period over which they determine the number of undersaturated days to about 1 month for their analyses. Nevertheless, the importance of exposure history found by Bednaršek et al. (2017) coupled to the existence of very long OAXs revealed by our study depicts a stressful environment for *L. helicina*, thus reducing their fitness in the CCS. More than 9% of the OAXs of the LLP cluster with undersaturated mean Ω_A conditions last longer than 1.5 yr, corresponding to the upper bound of pteropod *L. helicina*'s life-cycle (Bednaršek et al., 2017; Wang et al., 2017). In a worst case scenario of a pteropod becoming trapped into one of these events, this would mean that it would be exposed during its whole lifecycle to stressful Ω_A conditions, likely to hamper the spawning of a new generation. These results, although tentative, underscore the potential for severe impacts of OAX on marine life in the CCS.

4.4. Limitations and Caveats

Even though we evaluated our results as robust against several methodological choices, a number of limitations and potential caveats remain. Positive biases in the modeled chlorophyll-a concentration in the CCS nearshore surface waters in our model may lead to an underestimation of the number, intensity, duration, and extent of surface OAXs because overestimated biological productivity may buffer part of the upwelling-induced DIC variability in surface waters. Once the excess organic matter rains down to the sub-surface, overly strong remineralization could lead to an overestimation of sub-surface OAXs and of their intensity, as well as an overestimated number of OAXs with undersaturation conditions with regard to aragonite. However, in Section 3.4, we estimate the contribution of local biology to Ω_A anomalies in OAXs to be on average close to zero for ISC events (surface) and about a third for LLP and SMD events (sub-surface). The largely dominant contribution of physics to the Ω_A anomalies supports the fact that the identified chlorophyll bias is unlikely to affect our conclusions with regard to the drivers and spatial distribution of OAXs, as well as most of their properties.

With regard to the definition of the extremes in our study, a primary caveat is the use of a combined pH- Ω_A metric to define OAXs. While suitable for a range of organisms with a sensitivity to either or both carbonate chemistry variables (Bednaršek et al., 2019; Fabry et al., 2008; Kleypas et al., 1999; Kroeker et al., 2013; Manno et al., 2016), or for those where the driving variable of impact cannot be determined (Bach, 2015), our chosen metric is particularly useful for aragonite calcifying zooplankton species, such as pteropods that are known to be negatively impacted by both low pH and Ω_A (Bednaršek et al., 2014, 2019; Manno et al., 2016). Robustness assessments in Section 3.5 show that the majority of our results are robust to the choice of a dual or single variable extreme metric. In both cases, the identified OAXs have a similar spatial distribution and comparable characteristics, as well as a similar distribution among clusters, with the cluster of large, long, and propagating events remaining the cluster with the least but most severe events, mainly driven by cyclonic eddies. Other metrics, focusing on other carbonate system variables, or using absolute rather than relative thresholds may be suitable for other impact assessments. We believe that our flexible methodological framework is easily transferable to other systems, taxa or ecosystem functions, for instance to study the impact of combined pH- Ω_{Calcite} extremes on phytoplanktonic calcifiers (Kleypas et al., 2006; Kroeker et al., 2013), or to study cases where a single carbonate variable determines the exposure to extremes. Since the definition of criteria associated with ecosystem impacts

remains highly debated (Gruber et al., 2021), future work in the field is required to adapt our methodology for such use cases.

Furthermore, the tracking methodology we use may require some refinements. Some of the very long OAXs persist for months in the form of several cyclonic eddies that originate from the same coherent structure of grid-cells in extreme conditions, but can be spatially far apart. While the definition we use corresponds to a view where floating organisms remain trapped in these eddies, one could argue that the volume of these long extremes, because not spatially coherent anymore after a while, may only represent a reduced hazard for ecosystems compared to an equivalent volume of spatially coherent extreme conditions. We estimate that adding a criterion in the tracking method to split events once the branches are further apart than $\sim 1,400$ km from their joint center of gravity would lower the volume and duration of the five longest LLP events by respectively 4% and 11% on average. However, the critical distance as to when to split an event remains an unconstrained parameter and requires further research to motivate a certain choice.

Our assessment of the impact of OAXs on marine organisms is further limited by the absence of explicit calcifying phytoplankton and zooplankton groups in our version of the marine ecosystem model used in our study (BEC; Buitenhuis et al., 2019; Gangstø et al., 2011). Nevertheless, we estimated potential impacts on pteropods from the vertical extent, duration, and intensity of our OAX events using observational work by Bednaršek et al. (2014, 2017). Underlying this analysis is the assumption that pteropods remain trapped within an OAX from the beginning to the end of the event. Although pteropods drift along with currents, supporting the above assumption, they may not persistently remain trapped within extreme conditions, as they perform diurnal vertical migration (Bednaršek & Ohman, 2015). Estimated impacts may thus either be alleviated due to reduced exposure to extremes, or intensified as organisms become exposed to persistently lower pH or Ω_A at depth.

Last but not least, by focusing our analysis on events that occur at least once in the top 100 m, we do not take into account the impact of OAXs that occur at deeper depths only and potentially affect plankton such as pteropods during diel vertical migration (Hunt et al., 2008; Lalli & Gilmer, 1989; Mackas et al., 2005). While pteropods have been shown to migrate to depths of up to 250 m (Bednaršek & Ohman, 2015), most of the global pteropods biomass is found within the upper 100 m of the water column (Bednaršek et al., 2012). Furthermore, we found similar categories of OAXs with a similar distribution of characteristics when extending our analyses to events that occur within the top 250 m depth (Figures S17 and S18 in Supporting Information S1). In the latter case, LLP OAXs have deeper centers of gravity and deeper SMD OAXs occur offshore south of 35°N (Figure 7a and Figure S17 in Supporting Information S1). Characteristics of OAXs across clusters of events remain similar, except for a doubling of the LLPs median vertical extent, a lowering of the LLPs and SMDs median Ω_A as the events reach or occur deeper, and a decrease of median intensities by 28% on average (Figure 8 and Figure S18 in Supporting Information S1).

Hence, while we made specific choices as to the carbonate chemistry variables used, the depth regime and impact types considered, our results were robust to individual choices, and we believe that we could convincingly demonstrate that our methodology is transferable across extreme metrics, taxa, and study systems.

5. Summary and Conclusions

The differences in structure, strength, and propagation of the OAXs in the CCS are caused by the location and timing of the events and arise from the diversity of mechanisms involved in their formation (summary Figure 12). Although the leading role of coastal upwelling in generating OA extremes in the CCS was expected, the extensive involvement of mesoscale processes such as eddies in both the initiation and the persistence of those extremes, especially of the LLP, has substantial implications for the study of ocean extreme events at the global scale. We estimate that only 2% and 33% of the simulated extreme events in the CCS affect a sufficient area to be detected on a $1 \times 1^\circ$ or $0.25 \times 0.25^\circ$ grid, respectively. This implies that current global ocean biogeochemical models with a typical resolution of 1° are likely to miss a substantial fraction of potential OA extreme events by not resolving eddy dynamics.

The frequency, size, and magnitude of OAXs will likely increase under global climate change due to simultaneous changes in mean OA and in its variability. The predicted increase in upwelling strength in the future (Bakun, 1990; Diffenbaugh et al., 2003; Snyder et al., 2003; Xiu et al., 2018) may enhance the formation of ISC extremes

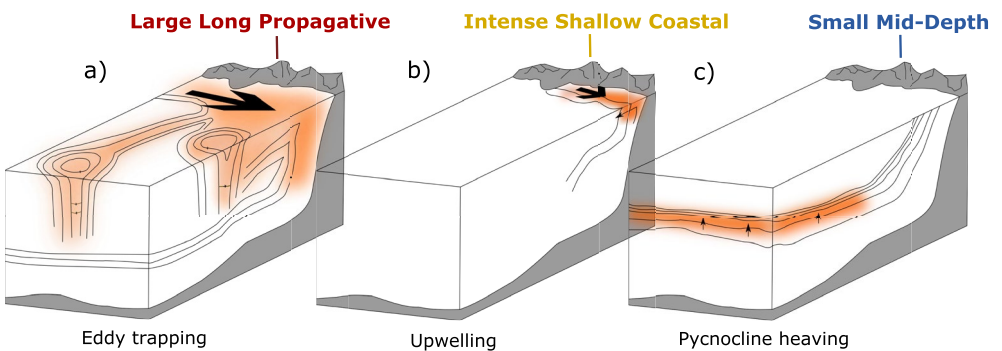


Figure 12. Diagram illustrating the spatial structure of the three types of extremes identified within the OAX events and their associated mechanisms. (a) The large, long, and propagating (LLP) events are mostly driven by eddies through trapping. (b) The intense, shallow, and coastal (ISC) events are driven by seasonal coastal upwelling. (c) The small and mid-depth (SMD) events result from pycnocline heaving.

(Lachkar, 2014). Concurrently, increased stratification associated with ocean warming may intensify ISC extremes through the deepening of isopycnals, which might induce upwelling of DIC-richer waters (Xiu et al., 2018). Understanding the temporal variability of the detected OAXs in concert with projected changes in their different drivers is crucial to better assess which level of OA stress CCS marine ecosystems will have to cope with.

The Lagrangian space-time identification of OA extremes opens new perspectives with regard to our understanding of the impact of extreme events on certain organisms such as the pteropod *L. helicina*. Coupling the results of our study to individual-based models may reveal some particularly damaging types of extremes (Hofmann Elizondo & Vogt, 2021). This knowledge together with an assessment of the temporal changes in OAXs will be highly relevant to comprehend how OA extremes may shape ecosystem structure, function, and health in the future (Gruber et al., 2021).

Appendix A: Estimation of OAXs Impact on Pteropods

We estimate potential shell dissolution in pteropod *L. helicina* individuals trapped into OAXs by using Equation A1 derived in Bednaršek et al. (2014).

$$y = \frac{e^{3.67x-1.66}}{1 + e^{3.67x-1.66}}, \quad (\text{A1})$$

where y is the proportion of pteropod *L. helicina* individuals with severe shell dissolution, and x is the percentage of undersaturated waters in the top 100 m of the water column. In our study, we approximate x by using the vertical extent (Table 1b) of OAXs that are in mean undersaturation conditions with regard to aragonite.

We further estimate the combined impact of the duration and the intensity of OAXs on the survival of pteropod *L. helicina* by defining an “undersaturation-days” metric (Equation A2) following Bednaršek et al. (2017).

$$S = I * D, \quad (\text{A2})$$

where we define D as the duration of an OAX in mean undersaturation conditions with regard to aragonite and I as its intensity relative to the absolute threshold of $\Omega_A = 1$. The undersaturation-days metric is then converted into a probability of survival using results in Figure 3 in Bednaršek et al. (2017).

Data Availability Statement

The code used to identify and track the OAX events and their properties in space and time can be obtained from <https://github.com/fDesmet/TRACEX>. All further analyses and all figures were created using the software package Python. The processed data are available online at the ETH library archive (<https://www.research-collection.ethz.ch/handle/20.500.11850/511215>). Model output data may be obtained upon request from the corresponding author (flora.desmet@usys.ethz.ch).

Acknowledgments

This research was supported by the Swiss National Science Foundation under grant agreement No 175787 (Project X-EBUS), by the Swiss Federal Institute of Technology Zürich (ETH Zürich), and by the European Union's Horizon 2020 research and innovation program under grant agreement No 820989 (project COMFORT). The simulations were performed at the HPC cluster of ETH Zürich, Euler, which is located in the Swiss Supercomputing Center (CSCS) in Lugano and operated by ETH ITS Scientific IT Services in Zürich. The authors would like to thank Dr. Luke Gregor, Dr. Fabio Benedetti, Urs Hofmann-Elizondo, Dr. Domitille Louchard, and Victor Boussange for the fruitful discussions, as well as Damian Loher for his technical support. The authors also thank the two reviewers for their thoughtful and constructive reviews that helped to improve the article. Open access funding provided by Eidgenössische Technische Hochschule Zurich.

References

- Amos, C. M., Castelao, R. M., & Medeiros, P. M. (2019). Offshore transport of particulate organic carbon in the California Current System by mesoscale eddies. *Nature Communications*, 10(1), 1–8. <https://doi.org/10.1038/s41467-019-12783-5>
- Bach, L. T. (2015). Reconsidering the role of carbonate ion concentration in calcification by marine organisms. *Biogeosciences*, 12, 4939–4951. <https://doi.org/10.5194/bg-12-4939-2015>
- Bakun, A. (1990). Global Climate Change and Intensification of Coastal Ocean Upwelling. *Science*, 247(4939), 198–201. <https://doi.org/10.1126/science.247.4939.198>
- Bates, N. R., Astor, Y. M., Church, M. J., Currie, K., Dore, J. E., González-Dávila, M., et al. (2014). A time-series view of changing surface ocean chemistry due to ocean uptake of anthropogenic CO₂ and ocean acidification. *Oceanography*, 27(1), 126–141. <https://doi.org/10.5670/oceanog.2014.16>
- Bednaršek, N., Feely, R. A., Howes, E. L., Hunt, B. P. V., Kessouri, F., León, P., et al. (2019). Systematic review and meta-analysis toward synthesis of thresholds of ocean acidification impacts on calcifying pteropods and interactions with warming. *Frontiers in Marine Science*, 6. <https://doi.org/10.3389/fmars.2019.00022>
- Bednaršek, N., Feely, R. A., Reum, J. C. P., Peterson, B., Menkel, J., Alin, S. R., & Hales, B. (2014). *Limacina helicina* shell dissolution as an indicator of declining habitat suitability owing to ocean acidification in the California current ecosystem. *Proceedings of the Royal Society B: Biological Sciences*, 281(1785), 20140123. <https://doi.org/10.1098/rspb.2014.0123>
- Bednaršek, N., Feely, R. A., Tolimieri, N., Hermann, A. J., Siedlecki, S. A., Waldbusser, G. G., et al. (2017). Exposure history determines pteropod vulnerability to ocean acidification along the U.S. West Coast. *Scientific Reports*, 7, 4526. <https://doi.org/10.1038/s41598-017-03934-z>
- Bednaršek, N., Harvey, C. J., Kaplan, I. C., Feely, R. A., & Možina, J. (2016). Pteropods on the edge: Cumulative effects of ocean acidification, warming, and deoxygenation. *Progress in Oceanography*, 145, 1–24. <https://doi.org/10.1016/j.pocean.2016.04.002>
- Bednaršek, N., Možina, J., Vogt, M., O'Brien, C., & Tarling, G. A. (2012). The global distribution of pteropods and their contribution to carbonate and carbon biomass in the modern ocean. *Earth System Science Data*, 4, 167–186. <https://doi.org/10.5194/essd-4-167-2012>
- Bednaršek, N., Naish, K.-A., Feely, R. A., Hauri, C., Kimoto, K., Hermann, A. J., et al. (2021). Integrated assessment of ocean acidification risks to pteropods in the northern high latitudes: Regional comparison of exposure, sensitivity, and adaptive capacity. *Frontiers in Marine Science*, 8, 1–23. <https://doi.org/10.3389/fmars.2021.671497>
- Bednaršek, N., & Ohman, M. D. (2015). Changes in pteropod distributions and shell dissolution across a frontal system in the California current system. *Marine Ecology Progress Series*, 523, 93–103. <https://doi.org/10.3354/meps11199>
- Bopp, L., Resplandy, L., Orr, J. C., Doney, S. C., Dunne, J. P., Gehlen, M., et al. (2013). Multiple stressors of ocean ecosystems in the 21st century: Projections with CMIP5 models. *Biogeosciences*, 10, 6225–6245. <https://doi.org/10.5194/bg-10-6225-2013>
- Buitenhuis, E. T., Le Quéré, C., Bednaršek, N., & Schiebel, R. (2019). Large contribution of pteropods to shallow CaCO₃ export. *Global Biogeochemical Cycles*, 33(3), 458–468. <https://doi.org/10.1029/2018GB006110>
- Buitenhuis, E. T., Vogt, M., Moriarty, R., Bednaršek, N., Doney, S. C., Leblanc, K., et al. (2013). MAREDAT: Towards a world atlas of MARine Ecosystem DATA. *Earth System Science Data*, 5(2), 227–239. <https://doi.org/10.5194/essd-5-227-2013>
- Burger, F., Frölicher, T., & John, J. (2020). Increase in ocean acidity variability and extremes under increasing atmospheric CO₂. *Biogeosciences Discussions*, 1–32. <https://doi.org/10.5194/bg-2020-22>
- Busch, D. S., & McElhany, P. (2016). Estimates of the direct effect of seawater pH on the survival rate of species groups in the California current ecosystem. *PLOS ONE*, 11(8). <https://doi.org/10.1371/journal.pone.0160669>
- Cai, W. J., Xu, Y. Y., Feely, R. A., Wanninkhof, R., Jönsson, B., Alin, S. R., et al. (2020). Controls on surface water carbonate chemistry along North American ocean margins. *Nature Communications*, 11(1), 1–13. <https://doi.org/10.1038/s41467-020-16530-z>
- Caliński, T., & Harabasz, J. (1974). A dendrite method for cluster analysis. *Communications in Statistics*, 3(1), 1–27. <https://doi.org/10.1080/03610927408827101>
- Carton, J. A., & Giese, B. S. (2008). A reanalysis of ocean climate using Simple Ocean Data Assimilation (SODA). *Monthly Weather Review*, 136(8), 2999–3017. <https://doi.org/10.1175/2007MWR1978.1>
- Chan, F., Barth, J. A., Blanchette, C. A., Byrne, R. H., Chavez, F., Cheriton, O., et al. (2017). Persistent spatial structuring of coastal ocean acidification in the California current system. *Scientific Reports*, 7(1), 2526. <https://doi.org/10.1038/s41598-017-02777-y>
- Chang, Y. L., & Oey, L. Y. (2014). Analysis of STCC eddies using the Okubo-Weiss parameter on model and satellite data. *Ocean Dynamics*, 64(2), 259–271. <https://doi.org/10.1007/s10236-013-0680-7>
- Chavez, F. P., & Messié, M. (2009). A comparison of eastern boundary upwelling ecosystems. *Progress in Oceanography*, 83(1–4), 80–96. <https://doi.org/10.1016/j.pocean.2009.07.032>
- Checkley, D. M., & Barth, J. A. (2009). Patterns and processes in the California current system. *Progress in Oceanography*, 83(1–4), 49–64. <https://doi.org/10.1016/j.pocean.2009.07.028>
- Chelton, D. B., Schlax, M. G., & Samelson, R. M. (2011). Global observations of nonlinear mesoscale eddies. *Progress in Oceanography*, 91(2), 167–216. <https://doi.org/10.1016/j.pocean.2011.01.002>
- Chenillat, F. (2015). Plankton dynamics in a cyclonic eddy in the Southern California current system. *Journal of Geophysical Research: Oceans*, 1–23. <https://doi.org/10.1002/2015JC010826>
- Chenillat, F., Franks, P. J., & Combes, V. (2016). Biogeochemical properties of eddies in the California current system. *Geophysical Research Letters*, 43(11), 5812–5820. <https://doi.org/10.1002/2016GL068945>
- Cohen, J. (1960). A coefficient of agreement for nominal scales. *Educational and Psychological Measurement*, XX(1), 37–46. <https://doi.org/10.1177/0013164460002000104>
- Comeau, S., Allouane, S., & Gattuso, J. P. (2012). Effects of ocean acidification on overwintering juvenile Arctic pteropods *Limacina helicina*. *Marine Ecology Progress Series*, 456, 279–284. <https://doi.org/10.3354/meps09696>
- Comeau, S., Gorsky, G., Allouane, S., & Gattuso, J. P. (2010). Larvae of the pteropod *Cavolinia inflexa* exposed to aragonite undersaturation are viable but shell-less. *Marine Biology*, 157(10), 2341–2345. <https://doi.org/10.1007/s00227-010-1493-6>
- Cooley, S. R., & Doney, S. C. (2009). Anticipating ocean acidification's economic consequences for commercial fisheries. *Environmental Research Letters*, 4(2), 024007. <https://doi.org/10.1088/1748-9326/4/2/024007>
- Copernicus Climate Change Service (C3S). (2017). ERA5: Fifth generation of ECMWF atmospheric reanalyses of the global climate. Copernicus Climate Change Service Climate Data Store (CDS). 29/08/2020.
- Cornwall, C. E., Comeau, S., DeCarlo, T. M., Larcombe, E., Moore, B., Giltrow, K., et al. (2020). A coralline alga gains tolerance to ocean acidification over multiple generations of exposure. *Nature Climate Change*, 10(2), 143–146. <https://doi.org/10.1038/s41558-019-0681-8>
- Cripps, G., Lindeque, P., & Flynn, K. J. (2014). Have we been underestimating the effects of ocean acidification in zooplankton? *Global Change Biology*, 20(11), 3377–3385. <https://doi.org/10.1111/gcb.12582>

- Davis, A., & Di Lorenzo, E. (2015). Interannual forcing mechanisms of California current transports II: Mesoscale eddies. *Deep-Sea Research Part II Topical Studies in Oceanography*, 112, 31–41. <https://doi.org/10.1016/j.dsr2.2014.02.004>
- Dickson, A. G., Sabine, C. L., & Christian, J. R. (2007). Guide to best practices for ocean CO₂ measurements. *PICES Special Publication*, 3(8), 191.
- Diffenbaugh, N. S., Snyder, M. A., & Sloan, L. C. (2003). Could CO₂-induced land-cover feedbacks alter near-shore upwelling regimes? *Proceedings of the National Academy of Sciences*, 101(1). <https://doi.org/10.1073/pnas.0305746101>
- Doney, S. C., Busch, D. S., Cooley, S. R., & Kroeker, K. J. (2020). The impacts of ocean acidification on marine ecosystems and reliant human communities. *Annual Review of Environment and Resources*, 1–30. <https://doi.org/10.1146/annurev-environ-012320-083019>
- Doney, S. C., Fabry, V. J., Feely, R. A., & Kleypas, J. A. (2009). Ocean acidification: The other CO₂ problem. *Annual Review of Marine Science*, 1(1), 169–192. <https://doi.org/10.1146/annurev.marine.010908.163834>
- Dufois, F., Hardman-Mountford, N. J., Greenwood, J., Richardson, A. J., Feng, M., & Matear, R. J. (2016). Anticyclonic eddies are more productive than cyclonic eddies in subtropical gyres because of winter mixing. *Science Advances*, 2(5), 1–7. <https://doi.org/10.1126/sciadv.1600282>
- Dussin, R., Barnier, B., Brodeau, L., & Molines, J. M. (2016). *The making of the Drakkar forcing set DFSS (Tech. Rep.)*. LGGE. Retrieved from <https://www.drakkar-ocean.eu/publications/reports>
- Ekstrom, J. A., Suatoni, L., Cooley, S. R., Pendleton, L. H., Waldbusser, G. G., Cinner, J. E., et al. (2015). Vulnerability and adaptation of US shellfisheries to ocean acidification. *Nature Climate Change*, 5(3), 207–214. <https://doi.org/10.1038/nclimate2508>
- Engström-Öst, J., Glippa, O., Feely, R. A., Kanerva, M., Keister, J. E., Alin, S. R., et al. (2019). Eco-physiological responses of copepods and pteropods to ocean warming and acidification. *Scientific Reports*, 9(1). <https://doi.org/10.1038/s41598-019-41213-1>
- Fabry, V. J., Seibel, B. A., Feely, R. A., & Orr, J. C. (2008). Impacts of ocean acidification on marine fauna and ecosystem processes. *ICES Journal of Marine Science*, 65, 414–432. <https://doi.org/10.1093/icesjms/fsn048>
- Fassbender, A. J., Alin, S. R., Feely, R. A., Sutton, A. J., Newton, J. A., Kremlis, C., et al. (2018). Seasonal carbonate chemistry variability in marine surface waters of the US Pacific Northwest. *Earth System Science Data*, 10, 1367–1401. <https://doi.org/10.5194/essd-10-1367-2018>
- Fassbender, A. J., Sabine, C. L., Feely, R. A., Langdon, C., & Mordy, C. W. (2011). Inorganic carbon dynamics during Northern California coastal upwelling. *Continental Shelf Research*. <https://doi.org/10.1016/j.csr.2011.04.006>
- Feely, R. A., Alin, S. R., Carter, B., Bednaršek, N., Hales, B., Chan, F., et al. (2016). Chemical and biological impacts of ocean acidification along the west coast of North America. *Estuarine, Coastal and Shelf Science*, 183, 260–270. <https://doi.org/10.1016/j.ecss.2016.08.043>
- Feely, R. A., Sabine, C. L., Byrne, R. H., Millero, F. J., Dickson, A. G., Wanninkhof, R., et al. (2012). Decadal changes in the aragonite and calcite saturation state of the Pacific Ocean. *Global Biogeochemical Cycles*, 26(3), 1–15. <https://doi.org/10.1029/2011GB004157>
- Feely, R. A., Sabine, C. L., Hernandez-Ayon, J. M., Ianson, D., & Hales, B. (2008). Evidence for upwelling of corrosive “acidified” water onto the continental shelf. *Science*, 320(5882), 1490–1492. <https://doi.org/10.1126/science.1155676>
- Franco, A. C., Gruber, N., Frölicher, T. L., & Kropuenske Artman, L. (2018). Contrasting impact of future CO₂ emission scenarios on the extent of CaCO₃ mineral undersaturation in the Humboldt Current System. *Journal of Geophysical Research: Oceans*, 123, 2018–2036. <https://doi.org/10.1002/2018JC013857>
- Frenger, I., Bianchi, D., Stührenberg, C., Oschlies, A., Dunne, J., Deutsch, C., et al. (2018). Biogeochemical role of subsurface coherent eddies in the ocean: Tracer cannonballs, hypoxic storms, and microbial stewpots? *Global Biogeochemical Cycles*, 32, 226–249. <https://doi.org/10.1002/2017GB005743>
- Frischknecht, M. (2018). *New perspectives on the three-dimensional cycling of carbon and nutrients in the California current system and its response to ENSO*. (Doctoral thesis). ETH Zürich. <https://doi.org/10.3929/ethz-b-000283522>
- Frischknecht, M., Münnich, M., & Gruber, N. (2018). Origin, transformation, and fate: The three-dimensional biological pump in the California current system. *Journal of Geophysical Research: Oceans*. <https://doi.org/10.1029/2018JC013934>
- Gangstø, R., Joos, F., & Gehlen, M. (2011). Sensitivity of pelagic calcification to ocean acidification. *Biogeosciences*, 8(2), 433–458. <https://doi.org/10.5194/bg-8-433-2011>
- García-Reyes, M., & Largier, J. (2010). Observations of increased wind-driven coastal upwelling off central California. *Journal of Geophysical Research*, 115(4), 1–8. <https://doi.org/10.1029/2009JC005576>
- GLOBALVIEW-CO₂. (2011). *Cooperative Atmospheric Data Integration Project-Carbon Dioxide*. CD-ROM, NOAA ESRL.
- Gregor, L., & Gruber, N. (2021). OceanSODA-ETHZ: A global gridded data set of the surface ocean carbonate system for seasonal to decadal studies of ocean acidification. *Earth System Science Data*, 13(2), 777–808. <https://doi.org/10.5194/essd-13-777-2021>
- Gruber, N., Boyd, P. W., Frölicher, T. L., & Vogt, M. (2021). Biogeochemical extremes and compound events in the ocean. *Nature*, 600(7889), 395–407. <https://doi.org/10.1038/s41586-021-03981-7>
- Gruber, N., Hauri, C., Lachkar, Z., Loher, D., Frölicher, T. L., & Plattner, G.-K. (2012). Rapid progression of ocean acidification in the California current system. *Science*, 337, 220–223. <https://doi.org/10.1126/science.1216773>
- Haigh, R., Ianson, D., Holt, C., Neate, H., & Edwards, A. (2015). Effects of ocean acidification on temperate coastal marine ecosystems and fisheries in the northeast Pacific. *PLOS One*, 10(2), e0117533. <https://doi.org/10.1371/journal.pone.0117533>
- Hauri, C., Friedrich, T., & Timmermann, A. (2015). Abrupt onset and prolongation of aragonite undersaturation events in the Southern Ocean. *Nature Climate Change*, 6(2). <https://doi.org/10.1038/nclimate2844>
- Hauri, C., Gruber, N., McDonnell, A. M. P., & Vogt, M. (2013). The intensity, duration, and severity of low aragonite saturation state events on the California continental shelf. *Geophysical Research Letters*, 40, 3424–3428. <https://doi.org/10.1002/grl.50618>
- Hauri, C., Gruber, N., Plattner, G.-K., Alin, S., Feely, R., Hales, B., & Wheeler, P. (2009). Ocean acidification in the California current system. *Oceanography*. <https://doi.org/10.5670/oceanog.2009.97>
- Hauri, C., Gruber, N., Vogt, M., Doney, S. C., Feely, R. A., Lachkar, Z., et al. (2013). Spatiotemporal variability and long-term trends of ocean acidification in the California current system. *Biogeosciences*, 10(1), 193–216. <https://doi.org/10.5194/bg-10-193-2013>
- Hauss, H., Christiansen, S., Schütte, F., Kiko, R., Lima, M. E., Rodrigues, E., et al. (2016). Dead zone or oasis in the open ocean? Zooplankton distribution and migration in low-oxygen mode-water eddies. *Biogeosciences*, 13(6), 1977–1989. <https://doi.org/10.5194/bg-13-1977-2016>
- Hersbach, H., Bell, B., Berrisford, P., Hirahara, S., Horányi, A., Muñoz-Sabater, J., et al. (2020). The ERA5 global reanalysis. *Quarterly Journal of the Royal Meteorological Society*, 146(730), 1999–2049. <https://doi.org/10.1002/qj.3803>
- Hobday, A. J., Alexander, L. V., Perkins, S. E., Smale, D. A., Straub, S. C., Oliver, E. C., et al. (2016). A hierarchical approach to defining marine heatwaves. *Progress in Oceanography*, 141, 227–238. <https://doi.org/10.1016/j.pocean.2015.12.014>
- Hofmann Elizondo, U., & Vogt, M. (2022). Individual-based modeling of shelled pteropods. *Ecological Modelling*, 468, 109944. <https://doi.org/10.1016/j.ecolmodel.2022.109944>
- Hunt, B. P., Pakhomov, E. A., Hosie, G. W., Siegel, V., Ward, P., & Bernard, K. (2008). Pteropods in Southern Ocean ecosystems. *Progress in Oceanography*, 78(3), 193–221. <https://doi.org/10.1016/j.pocean.2008.06.001>

- Jacox, M. G., Edwards, C. A., Hazen, E. L., & Bograd, S. J. (2018). Coastal upwelling revisited: Ekman, Bakun, and improved upwelling indices for the U.S. West Coast. *Journal of Geophysical Research: Oceans*. <https://doi.org/10.1029/2018JC014187>
- Jiang, L. Q., Carter, B. R., Feely, R. A., Lauvset, S. K., & Olsen, A. (2019). Surface ocean pH and buffer capacity: Past, present, and future. *Scientific Reports*, 9(1), 1–11. <https://doi.org/10.1038/s41598-019-55039-4>
- Kleypas, J. A., Buddemeier, R. W., Archer, D., Gattuso, J. P., Langdon, C., & Opdyke, B. N. (1999). Geochemical consequences of increased atmospheric carbon dioxide on coral reefs. *Science*, 284(5411). <https://doi.org/10.1126/science.284.5411.118>
- Kleypas, J. A., Feely, R., Fabry, V., Langdon, C., Sabine, C., & Robbins, L. (2006). *Impacts of Ocean Acidification on Coral Reefs and Other Marine Calcifiers: A guide for future research*. Report of a workshop sponsored by NSF, NOAA, and the U.S. Geological Survey, 88.
- Kroeker, K. J., Bell, L. E., Donham, E. M., Hoshijima, U., Lummis, S., Toy, J. A., & Willis-Norton, E. (2020). Ecological change in dynamic environments: Accounting for temporal environmental variability in studies of ocean change biology. *Global Change Biology*, 26, 54–67. <https://doi.org/10.1111/gcb.14868>
- Kroeker, K. J., Kordas, R. L., Crim, R., Hendriks, I. E., Ramajo, L., Singh, G. S., et al. (2013). Impacts of ocean acidification on marine organisms: Quantifying sensitivities and interaction with warming. *Global Change Biology*, 19(6), 1884–1896. <https://doi.org/10.1111/gcb.12179>
- Kroeker, K. J., Kordas, R. L., Crim, R. N., & Singh, G. G. (2010). Meta-analysis reveals negative yet variable effects of ocean acidification on marine organisms. *Ecology Letters*, 13(11), 1419–1434. <https://doi.org/10.1111/j.1461-0248.2010.01518.x>
- Kruskal, W. H., & Wallis, W. A. (1952). Use of ranks in one-criterion variance analysis. *Journal of the American Statistical Association*, 47(260), 583–621. <https://doi.org/10.1080/01621459.1952.10483441>
- Kurian, J., Colas, F., Capet, X., McWilliams, J. C., & Chelton, D. B. (2011). Eddy properties in the California current system. *Journal of Geophysical Research*, 116(C8), C08027. <https://doi.org/10.1029/2010JC006895>
- Kwiatkowski, L., & Orr, J. C. (2018). Diverging seasonal extremes for ocean acidification during the 21st century. *Nature Climate Change*, 8, 141–145. <https://doi.org/10.1038/s41558-017-0054-0>
- Lachkar, Z. (2014). Effects of upwelling increase on ocean acidification in the California and Canary current systems. *Geophysical Research Letters*, 41(1), 90–95. <https://doi.org/10.1002/2013GL058726>
- Lalli, C. M., & Gilmer, R. W. (1989). *Pelagic snails: The biology of holoplanktonic gastropod mollusks*. Stanford University Press.
- Landis, J. R., & Koch, G. G. (1977). The measurement of observer agreement for categorical data. *Biometrics*, 33(1), 159. <https://doi.org/10.2307/2529310>
- Landschützer, P., Laruelle, G. G., Roobaert, A., & Regnier, P. (2020). A uniform pCO₂ climatology combining open and coastal oceans. *Earth System Science Data*, 12(4), 2537–2553. <https://doi.org/10.5194/essd-12-2537-2020>
- Large, W. G., McWilliams, J. C., & Doney, S. C. (1994). Oceanic vertical mixing: A review and a model with a nonlocal boundary layer parameterization. *Reviews of Geophysics*, 32(4), 363–403. <https://doi.org/10.1029/94RG01872>
- Lauvset, S. K., Gruber, N., Landschützer, P., Olsen, A., & Tjiputra, J. (2015). Trends and drivers in global surface ocean pH over the past three decades. *Biogeosciences*, 12(5), 1285–1298. <https://doi.org/10.5194/bg-12-1285-2015>
- Lauvset, S. K., Key, R. M., Olsen, A., Van Heege, S., Velo, A., Lin, X., et al. (2016). A new global interior ocean mapped climatology: The 1° × 1° GLODAP version 2. *Earth System Science Data*. <https://doi.org/10.5194/essd-8-325-2016>
- Leinweber, A., & Gruber, N. (2013). Variability and trends of ocean acidification in the Southern California current system: A time series from Santa Monica Bay. *Journal of Geophysical Research: Oceans*, 118(7), 3622–3633. <https://doi.org/10.1002/jgrc.20259>
- Lohbeck, K. T., Riebesell, U., & Reusch, T. B. (2012). Adaptive evolution of a key phytoplankton species to ocean acidification. *Nature Geoscience*, 5(5), 346–351. <https://doi.org/10.1038/ngeo1441>
- Lovecchio, E., Gruber, N., & Münnich, M. (2018). Mesoscale contribution to the long-range offshore transport of organic carbon from the Canary upwelling system to the open North Atlantic. *Biogeosciences*, 15, 5061–5091. <https://doi.org/10.5194/bg-15-5061-2018>
- Lovecchio, E., Gruber, N., Münnich, M., & Frenger, I. (2022). On the processes sustaining biological production in the offshore propagating eddies of the northern Canary upwelling system. *Journal of Geophysical Research: Oceans*, 1–39. <https://doi.org/10.1029/2021jc017691>
- Lovecchio, E., Gruber, N., Münnich, M., & Lachkar, Z. (2017). On the long-range offshore transport of organic carbon from the Canary upwelling system to the open North Atlantic. *Biogeosciences*, 14(13), 3337–3369. <https://doi.org/10.5194/bg-14-3337-2017>
- Lueker, T. J., Dickson, A. G., & Keeling, C. D. (2000). Ocean pCO₂ calculated from dissolved inorganic carbon, alkalinity, and equations for K1 and K2: Validation based on laboratory measurements of CO₂ in gas and seawater at equilibrium. *Marine Chemistry*, 70(1–3), 105–119. [https://doi.org/10.1016/S0304-4203\(00\)00022-0](https://doi.org/10.1016/S0304-4203(00)00022-0)
- Mackas, D. L., Tsurumi, M., Galbraith, M. D., & Yelland, D. R. (2005). Zooplankton distribution and dynamics in a North Pacific eddy of coastal origin: II. Mechanisms of eddy colonization by and retention of offshore species. *Deep-Sea Research Part II Topical Studies in Oceanography*, 52(7–8), 1011–1035. <https://doi.org/10.1016/j.dsr2.2005.02.008>
- Manno, C., Bednaršek, N., Tarling, G. A., Peck, V. L., Comeau, S., Adhikari, D., et al. (2017). Shelled pteropods in peril: Assessing vulnerability in a high CO₂ ocean. *Earth-Science Reviews*, 169, 132–145. <https://doi.org/10.1016/j.earscirev.2017.04.005>
- Manno, C., Morata, N., & Primicerio, R. (2012). *Limacina retroversa*'s response to combined effects of ocean acidification and sea water freshening. *Estuarine, Coastal and Shelf Science*, 113, 163–171. <https://doi.org/10.1016/j.ecss.2012.07.019>
- Manno, C., Peck, V. L., & Tarling, G. A. (2016). Pteropod eggs released at high pCO₂ lack resilience to ocean acidification. *Scientific Reports*, 6, 1–10. <https://doi.org/10.1038/srep25752>
- Marchesello, P., McWilliams, J. C., & Shcherbakov, A. (2003). Equilibrium structure and dynamics of the California current system. *Journal of Physical Oceanography*, 33(4), 753–783. [https://doi.org/10.1175/1520-0485\(2003\)33<753:esadot>2.0.co;2](https://doi.org/10.1175/1520-0485(2003)33<753:esadot>2.0.co;2)
- Marshall, K. N., Kaplan, I. C., Hodgson, E. E., Hermann, A., Busch, D. S., McElhany, P., et al. (2017). Risks of ocean acidification in the California current food web and fisheries: Ecosystem model projections. *Global Change Biology*, 23(4), 1525–1539. <https://doi.org/10.1111/gcb.13594>
- Mekkes, L., Renema, W., Bednaršek, N., Alin, S. R., Feely, R. A., Huisman, J., et al. (2021). Pteropods make thinner shells in the upwelling region of the California current ecosystem. *Scientific Reports*, 11(1731), 1–11. <https://doi.org/10.1038/s41598-021-81131-9>
- Messié, M., Ledesma, J., Kolber, D. D., Michisaki, R. P., Foley, D. G., & Chavez, F. P. (2009). Potential new production estimates in four eastern boundary upwelling ecosystems. *Progress in Oceanography*, 83(1–4), 151–158. <https://doi.org/10.1016/j.pocean.2009.07.018>
- Moore, J. K., Doney, S. C., Kleypas, J. A., Glover, D. M., & Fung, I. Y. (2002). An intermediate complexity marine ecosystem model for the global domain. *Deep-Sea Research Part II: Topical Studies in Oceanography*, 49, 403–462. [https://doi.org/10.1016/S0967-0645\(01\)00108-4](https://doi.org/10.1016/S0967-0645(01)00108-4)
- Moore, J. K., Lindsay, K., Doney, S. C., Long, M. C., & Misumi, K. (2013). Marine ecosystem dynamics and biogeochemical cycling in the Community Earth system model [CESM1(BGC)]: Comparison of the 1990s with the 2090s under the RCP4.5 and RCP8.5 scenarios. *Journal of Climate*, 26, 9291–9312. <https://doi.org/10.1175/JCLI-D-12-00566.1>

- Nagai, T., Gruber, N., Frenzel, H., Lachkar, Z., McWilliams, J. C., & Plattner, G. K. (2015). Dominant role of eddies and filaments in the offshore transport of carbon and nutrients in the California current system. *Journal of Geophysical Research: Oceans*. <https://doi.org/10.1002/2015JC010889>
- Okubo, A. (1970). Horizontal dispersion of floatable particles in the vicinity of velocity singularities such as convergences. *Deep-Sea Research and Oceanographic Abstracts*, 17(3), 445–454. [https://doi.org/10.1016/0011-7471\(70\)90059-8](https://doi.org/10.1016/0011-7471(70)90059-8)
- Oliver, E. C., Benthuysen, J. A., Darmaraki, S., Donat, M. G., Hobday, A. J., Holbrook, N. J., et al. (2021). Marine heatwaves. *Annual Review of Marine Science*, 13, 313–342. <https://doi.org/10.1146/annurev-marine-032720-095144>
- Orr, J. C., & Epitalon, J. M. (2015). Improved routines to model the ocean carbonate system: Mocsy 2.0. *Geoscientific Model Development*, 8(3), 485–499. <https://doi.org/10.5194/gmd-8-485-2015>
- Orr, J. C., Fabry, V. J., Aumont, O., Bopp, L., Doney, S. C., Feely, R. A., et al. (2005). Anthropogenic ocean acidification over the 21st century and its impact on calcifying organisms. *Nature*, 437(7059), 681–686. <https://doi.org/10.1038/nature04095>
- Osborne, E. B., Thunell, R. C., Gruber, N., Feely, R. A., & Benitez-Nelson, C. R. (2020). Decadal variability in 20th century ocean acidification in the California current ecosystem. *Nature Geoscience*, 13(1), 43–49. <https://doi.org/10.1038/s41561-019-0499-z>
- Palacios, D. M., Bograd, S. J., Mendelsohn, R., & Schwing, F. B. (2004). Long-term and seasonal trends in stratification in the California current, 1950–1993. *Journal of Geophysical Research C: Oceans*, 109(10), 1–12. <https://doi.org/10.1029/2004JC002380>
- Pauly, D., & Christensen, V. (1995). Primary production required to sustain global fisheries. *Nature*, 374, 255–257. <https://doi.org/10.1038/374255a0>
- Pedregosa, F., Varoquaux, G., Gramfort, A., Michel, V., Thirion, B., Grisel, O., et al. (2011). Scikit-learn: Machine learning in Python. *Journal of Machine Learning Research*, 12, 2825–2830.
- Perez, F. F., & Fraga, F. (1987). Association constant of fluoride and hydrogen ions in seawater. *Marine Chemistry*, 21(2), 161–168. [https://doi.org/10.1016/0304-4203\(87\)90036-3](https://doi.org/10.1016/0304-4203(87)90036-3)
- Reynolds, R. W., Smith, T. M., Liu, C., Chelton, D. B., Casey, K. S., & Schlax, M. G. (2007). Daily high-resolution-blended analyses for sea surface temperature. *Journal of Climate*, 20(22), 5473–5496. <https://doi.org/10.1175/2007JCLI1824.1>
- Riebesell, U., & Gattuso, J. P. (2015). Lessons learned from ocean acidification research. *Nature Climate Change*, 5(1), 12–14. <https://doi.org/10.1038/nclimate2456>
- Rivest, E. B., Comeau, S., & Cornwall, C. E. (2017). The role of natural variability in shaping the response of coral reef organisms to climate change. *Current Climate Change Reports*, 3(4), 271–281. <https://doi.org/10.1007/s40641-017-0082-x>
- Rousseeuw, P. J. (1987). Silhouettes: A graphical aid to the interpretation and validation of cluster analysis. *Journal of Computational and Applied Mathematics*, 20, 53–65. [https://doi.org/10.1016/0377-0427\(87\)90125-7](https://doi.org/10.1016/0377-0427(87)90125-7)
- Sabine, C. L., Feely, R. A., Gruber, N., Key, R. M., Lee, K., Bullister, J. L., et al. (2004). The oceanic sink for anthropogenic CO₂. *Science*, 305(5682), 367–371. <https://doi.org/10.1126/science.1097403>
- Seifert, M., Rost, B., Trimborn, S., & Hauck, J. (2020). Meta-analysis of multiple driver effects on marine phytoplankton highlights modulating role of pCO₂. *Global Change Biology*, 26(12), 6787–6804. <https://doi.org/10.1111/gcb.15341>
- Shchepetkin, A. F., & McWilliams, J. C. (2005). The regional oceanic modeling system (ROMS): A split-explicit, free-surface, topography-following-coordinate oceanic model. *Ocean Modeling*, 9(4), 347–404. <https://doi.org/10.1016/j.ocemod.2004.08.002>
- Snyder, M. A., Sloan, L. C., Diffenbaugh, N. S., & Bell, J. L. (2003). Future climate change and upwelling in the California current. *Geophysical Research Letters*, 30(15), 1–4. <https://doi.org/10.1029/2003GL017647>
- Spisla, C., Taucher, J., Bach, L. T., Haunost, M., Boxhammer, T., King, A. L., et al. (2021). Extreme levels of ocean acidification restructure the plankton community and biogeochemistry of a temperate coastal ecosystem: A mesocosm study. *Frontiers in Marine Science*, 7, 1–24. <https://doi.org/10.3389/fmars.2020.611157>
- Strub, P. T., & James, C. (1995). The large-scale summer circulation of the California current. *Geophysical Research Letters*, 22(3), 207–210. <https://doi.org/10.1029/94GL03011>
- Strub, P. T., Kosro, P. M., & Huyer, A. (1991). The nature of the cold filaments in the California current system. *Journal of Geophysical Research*, 96(C8), 14743. <https://doi.org/10.1029/91jc01024>
- Sutton, A. J., Feely, R. A., Maenner-Jones, S., Musielowicz, S., Osborne, J., Dietrich, C., et al. (2019). Autonomous seawater pCO₂ and pH time series from 40 surface buoys and the emergence of anthropogenic trends. *Earth System Science Data*, 11(1), 421–439. <https://doi.org/10.5194/essd-11-421-2019>
- Torres, O., Kwiatkowski, L., Sutton, A. J., Dorey, N., & Orr, J. C. (2021). Characterizing mean and extreme diurnal variability of ocean CO₂ system variables across marine environments. *Geophysical Research Letters*, 48(5), 1–12. <https://doi.org/10.1029/2020GL090228>
- Turi, G., Lachkar, Z., & Gruber, N. (2014). Spatiotemporal variability and drivers of pCO₂ and air-sea CO₂ fluxes in the California current system: An eddy-resolving modeling study. *Biogeosciences*, 11, 671–690. <https://doi.org/10.5194/bg-11-671-2014>
- Turi, G., Lachkar, Z., Gruber, N., & Münnich, M. (2016). Climatic modulation of recent trends in ocean acidification in the California current system. *Environmental Research Letters*, 11, 1–17. <https://doi.org/10.1088/1748-9326/11/1/014007>
- Uppström, L. R. (1974). The boron/chlorinity ratio of deep-sea water from the Pacific Ocean. *Deep-Sea Research and Oceanographic Abstracts*, 21(2), 161–162. [https://doi.org/10.1016/0011-7471\(74\)90074-6](https://doi.org/10.1016/0011-7471(74)90074-6)
- Vargas, C. A., Lagos, N. A., Lardies, M. A., Duarte, C., Maríñez, P. H., Aguilera, V. M., et al. (2017). Species-specific responses to ocean acidification should account for local adaptation and adaptive plasticity. *Nature Ecology and Evolution*, 1(4), 1–7. <https://doi.org/10.1038/s41559-017-0084>
- Wang, K., Hunt, B. P., Liang, C., Pauly, D., & Pakhomov, E. A. (2017). Reassessment of the life cycle of the pteropod *Limacina helicina* from a high-resolution interannual time series in the temperate North Pacific. *ICES Journal of Marine Science*, 74(7), 1906–1920. <https://doi.org/10.1093/icesjms/fsx014>
- Weaver, J. R. (1985). Centrosymmetric (cross-symmetric) matrices, their basic properties, eigenvalues, and eigenvectors. *The American Mathematical Monthly*, 92(10), 711–717. <https://doi.org/10.1080/00029890.1985.11971719>
- Weiss, J. (1991). The dynamics of enstrophy transfer in two-dimensional hydrodynamics. *Physica D: Nonlinear Phenomena*, 48(2–3), 273–294. [https://doi.org/10.1016/0167-2789\(91\)90088-Q](https://doi.org/10.1016/0167-2789(91)90088-Q)
- Wilks, D. S. (2011). *Statistical methods in the atmospheric sciences* (3rd ed.). A. Academic Press.
- Xiu, P., Chai, F., Curchitser, E. N., & Castruccio, F. S. (2018). Future changes in coastal upwelling ecosystems with global warming: The case of the California current system. *Scientific Reports*, 8(1), 2866. <https://doi.org/10.1038/s41598-018-21247-7>
- Xue, L., Cai, W., Jiang, L., & Wei, Q. (2021). Why are surface ocean pH and CaCO₃ saturation state often out of phase in spatial patterns and seasonal cycles? *Global Biogeochemical Cycles*, 1–16. <https://doi.org/10.1029/2021gb006949>